J. Fluid Mech. (2022), *vol*. 950, A22, doi:10.1017/jfm.2022.773

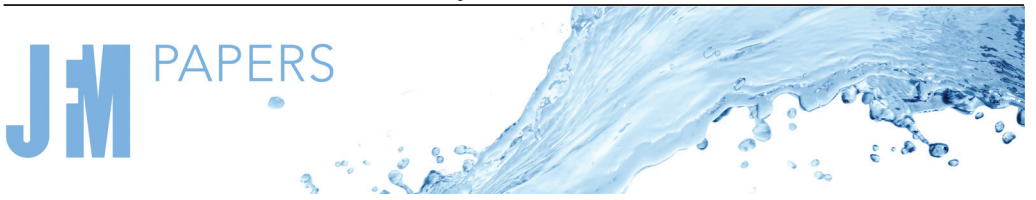

The effect of spanwise heterogeneous surfaces on mixed convection in turbulent channels

Kay Schäfer[1],†, **Bettina Frohnapfel**[1] **and Juan Pedro Mellado**[2]

[1]Institute of Fluid Mechanics, Karlsruhe Institute of Technology, 76131 Karlsruhe, Germany

[2]Meteorological Institute, University of Hamburg, 20146 Hamburg, Germany

(Received 18 March 2022; revised 2 August 2022; accepted 4 September 2022)

Turbulent mixed convection in channel flows with heterogeneous surfaces is studied using direct numerical simulations. The relative importance of buoyancy and shear effects, characterised by the bulk Richardson number Ri_b, is varied in order to cover the flow regimes of forced, mixed and natural convection, which are associated with different large-scale flow organisations. The heterogeneous surface consists of streamwise-aligned ridges, which are known to induce secondary motion in the case of forced convection. The large-scale streamwise rolls emerging under smooth-wall mixed convection conditions are significantly affected by the heterogeneous surfaces and their appearance is considerably reduced for dense ridge spacings. It is found that the formation of these rolls requires larger buoyancy forces than over smooth walls due to the additional drag induced by the ridges. Therefore, the transition from forced convection structures to rolls is delayed towards larger Ri_b for spanwise heterogeneous surfaces. The influence of the heterogeneous surface on the flow organisation of mixed convection is particularly pronounced in the roll-to-cell transition range, where ridges favour the transition to convective cells at significantly lower Ri_b. In addition, the convective cells are observed to align perpendicular to the ridges with decreasing ridge spacing. We attribute this reorganisation to the fact that flow parallel to the ridges experience less drag than flow across the ridges, which is energetically more beneficial. Furthermore, we find that streamwise rolls exhibit a very slow dynamics for $Ri_b = 1$ and $Ri_b = 3.2$ when the ridge spacing is of the order of the rolls' width. For these cases the up- and downdrafts of the rolls move slowly across the entire channel instead of being fixed in space, as observed for the smooth-wall cases.

Key words: turbulent convection, boundary layer structure, topographic effects

† Email address for correspondence: kay.schaefer@kit.edu

1. Introduction

In many technical and environmental flows, shear and buoyancy effects occur simultaneously and both may significantly contribute to the heat and mass transfer of the flow. This transport process, also known as mixed convection, represents the combination of the two extreme cases of forced and natural convection, where the former is driven purely by a pressure gradient and the latter by vertical temperature differences. While in forced convection turbulence is produced by shear and in natural convection by buoyancy, both effects contribute to turbulence production in mixed convection flows. The aforementioned flows often occur over rough surfaces, which can also strongly influence the flow properties. In the forced convection community, heterogeneous rough surfaces have received special attention in recent years, since in turbulent wall-bounded flows they can induce secondary flows of Prandtl's second kind that can significantly change the transport properties of the flow. It is therefore the objective of the present study to investigate the effects of heterogeneous surfaces on the interplay of forced and natural convection in turbulent flows.

In mixed convection flows with unstable thermal stratification, where denser fluid is bedded over less dense fluid, different turbulent large-scale flow structures have been identified and the organisation depends on the relative strength between shear and buoyancy effects, such as in turbulent channel flows (Pirozzoli *et al.* 2017), turbulent Couette flows (Blass *et al.* 2020) and in the atmospheric boundary layer (ABL) (Deardorff 1972; LeMone 1973; Moeng & Sullivan 1994; Khanna & Brasseur 1998). The transition between different flow organisations is accompanied by an alteration of the effective heat and momentum transfer in the flow. In the case of strong buoyancy effects and weak shear, open cells form in the flow, which resemble Rayleigh–Bénard convection, while in the case of weak to moderate buoyancy effects and strong shear, the flow organises into horizontal rolls aligned with the main flow direction (Khanna & Brasseur 1998; Pirozzoli *et al.* 2017; Salesky, Chamecki & Bou-Zeid 2017). These streamwise rolls are illustrated in the cross-sectional plane of the channel in figure 1(*a*), with the up- and downdraft region of the roll occurring where localised buoyancy forces accumulate. At very strong shear, with negligible buoyancy effects, the flow organisation in turbulent channels resembles that of classical Poiseuille flows (Pirozzoli *et al.* 2017) and in the case of neutral ABL that of flat-plate boundary layers (Khanna & Brasseur 1998).

The transition between the different flow topologies of mixed convection can be characterised by various stability parameters. In the atmospheric science community, the stability parameter $-z_i/L$ is used to classify the transitions between rolls and cellular structures, which expresses the ratio of the boundary layer depth z_i and the Obukhov length L. The Monin–Obukhov similarity theory introduces the Obukhov length L as a length scale that compares the effects of friction and buoyancy on the flow; L is used for non-dimensionalisation to generalise Prandtl's mixing length theory for buoyancy effects of non-neutral stratifications (Obukhov 1946; Monin & Obukhov 1954; Wyngaard 2010). In this context, $|L|$ can be physically interpreted as the height at which the buoyant production of turbulent kinetic energy equals that due to shear production, such that below $|L|$ mechanical production predominates, while above $|L|$ buoyant production is dominant. In the case of convective boundary layers, large ratios of $-z_i/L$ are indicative of the formation of convective cells, while small values are typical for roll formation (Khanna & Brasseur 1998; Salesky *et al.* 2017). An alternative stability parameter to characterise the relative importance of buoyancy effects and shear is the Richardson number Ri. For mixed convection in turbulent channel flows, low Ri corresponds to pure forced convection, intermediate values of Ri to roll formation and large Ri values to natural convection with

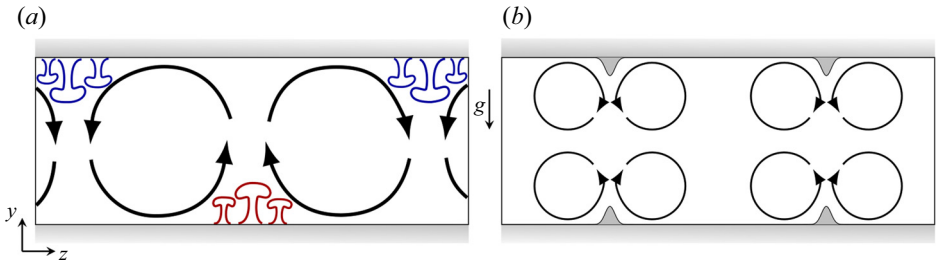

Figure 1. Schematic of different large-scale structures in the cross-sectional plane. In (*a*) streamwise rolls can emerge in flows with buoyancy effects over smooth walls, while in (*b*) secondary motions appear over rough walls in form of streamwise-aligned ridges. The direction of gravitational acceleration g is given by the downward arrow.

cell-like structures (Pirozzoli *et al.* 2017). Independent of the chosen stability parameter the exact range at which the transition between the different flow regimes occurs is still under debate with recent studies focusing on the transition between rolls and cells (Salesky *et al.* 2017) and the transition between neutral to moderately convective conditions (Jayaraman & Brasseur 2021).

Effects of surface heterogeneity, occurring for instance between urban–rural areas, on the transition between the different flow organisations in mixed convection has gained little attention, even though their impact on the quality of weather and climate prediction is important (Bou-Zeid *et al.* 2020). Likewise, there is the chance that the flow topology may have an influence on the deformation of the surface topography, which in turn affects the flow and possibly results in a positive feedback. For example, from satellite observations of deserts in the 1960s, it was proposed that quasi-streamwise rolls in the ABL were responsible for the formation of sand dunes aligned with the mean flow direction (Hanna 1969; Shao 2008). This is similar to observations from aqueous open-channel flows, where sand dunes can also form due to a positive feedback with large-scale flow structures. The formation of these large-scale flow structures is associated with irregularities in the surface topography, which leads to the formation of so-called secondary motions (Colombini 1993; Scherer *et al.* 2022), which, unlike the streamwise rolls, can occur without buoyancy effects.

These secondary motions, also named secondary motions of Prandtl's second kind (Hinze 1973; Anderson *et al.* 2015), can occur in turbulent flows over surfaces with spanwise variations in the wall properties, which can significantly alter the momentum and heat transport of turbulent flows (Stroh *et al.* 2020*a*). Unlike streamwise rolls, secondary motions cannot be observed in instantaneous velocity fields, instead they occur only in time-averaged velocity fields, where they appear as counter-rotating vortices aligned with the main flow direction. The secondary motions introduce a spanwise variation in the mean velocity field, which, for instance in a turbulent boundary layer, leads to spanwise modulation of the boundary layer thickness (Willingham *et al.* 2014). These differences in the mean profile are associated with the formation of low- and high-momentum pathways in the mean velocity field, usually occurring at the updraft and downdraft regions of the secondary motions, respectively (Barros & Christensen 2014; Willingham *et al.* 2014).

The spanwise heterogeneous surfaces, triggering secondary motions, are roughly distinguished in two main surface types, namely in ridge-type and strip-type roughnesses (Wang & Cheng 2006). Strip-type roughness is characterised by significant spanwise differences in drag, for example alternating streamwise strips with different wall-shear

stress conditions (Willingham *et al.* 2014; Anderson *et al.* 2015; Chung, Monty & Hutchins 2018) or alternating strips of smooth and rough walls, which do not feature large differences in the wall elevation (Hinze 1973; Stroh *et al.* 2020*b*; Wangsawijaya *et al.* 2020; Schäfer *et al.* 2022). Ridge-type roughness comprises notable spanwise wall elevation differences, such as streamwise-aligned ridges, which are studied numerically and experimentally for a wide range of different ridge shapes in turbulent boundary layers (Vanderwel & Ganapathisubramani 2015; Hwang & Lee 2018; Medjnoun, Vanderwel & Ganapathisubramani 2018; Vanderwel *et al.* 2019; Medjnoun, Vanderwel & Ganapathisubramani 2020), turbulent channel flows (Vanderwel *et al.* 2019; Stroh *et al.* 2020*a*) and turbulent open-channel flows (Awasthi & Anderson 2018; Zampiron, Cameron & Nikora 2020).

The ridge-type behaviour of secondary motions is characterised by updraft regions occurring above the centre ridge position, while downdrafts descend in the valley region between adjacent ridges, as illustrated in figure 1(*b*). The spanwise distance between the ridges influences the spatial extent of the secondary motion (Vanderwel & Ganapathisubramani 2015; Vanderwel *et al.* 2019). For large ridge spacings, which are of the order of several boundary layer thicknesses, the flow is divided into regions disturbed by the secondary motion in the vicinity of the ridge and a homogeneous and unaffected region far from the ridges. In the case of ridge spacings of the order of the boundary layer thickness, the secondary motion affects the entire flow region and introduces a spanwise heterogeneity into the mean flow (Hwang & Lee 2018; Medjnoun *et al.* 2020). Further reduction of the ridge spacing leads to a decreasing spatial extent of the secondary motions, which scales with the ridge spacing.

The objective of the present study is to investigate the influence of spanwise heterogeneous surfaces on turbulent mixed convection flows as well as their influence on the transition between the different large-scale flow organisations. Secondary motions feature, in a mean sense, some similarities to the roll motion of mixed convection, e.g. large-scale counter-rotating vortices, as depicted in figure 1. Since secondary motions can be induced by streamwise-aligned ridges, the study investigates to which extent such surface structures can influence the formation and dynamics of streamwise rolls. These questions are investigated using a simplified setting of a turbulent channel flow, similar to that of Pirozzoli *et al.* (2017), augmented with streamwise-aligned ridges on the walls. The different flow regimes of mixed convection are covered by systematically varying the relative strengths of shear and buoyancy effects.

2. Methodology

2.1. *Flow configuration and numerical procedure*

The balance equations for mass, momentum and energy are considered in the Boussinesq approximation

$$\frac{\partial u_i}{\partial x_i} = 0, \tag{2.1}$$

$$\frac{\partial u_i}{\partial t} + \frac{\partial u_i u_j}{\partial x_j} = -\frac{1}{\rho_0}\frac{\partial p}{\partial x_i} + \nu\frac{\partial^2 u_i}{\partial x_j \partial x_j} + \beta g T \delta_{i2} + \Pi\delta_{i1} + F_{IBM,i}, \tag{2.2}$$

$$\frac{\partial T}{\partial t} + \frac{\partial T u_j}{\partial x_j} = \alpha\frac{\partial^2 T}{\partial x_j \partial x_j} + Q_{IBM}, \tag{2.3}$$

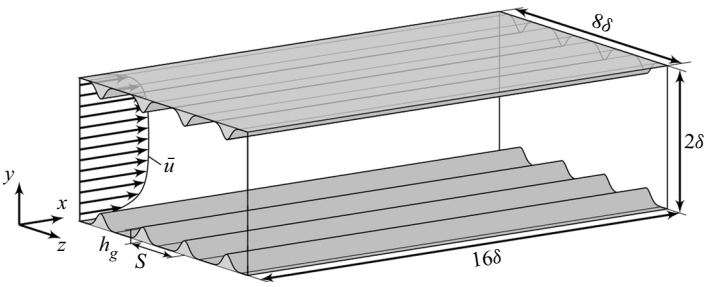

Figure 2. Sketch of the numerical channel domain with streamwise-aligned Gaussian ridges at the walls.

where u_i and x_i are the components of the velocity and position vector, with indices 1, 2, 3 corresponding to the streamwise, wall-normal and spanwise directions. As an index-free notation, the velocity components are also written as $(u, v, w) = (u_1, u_2, u_3)$. The reference density is given by ρ_0, p is the pressure, ν the kinematic viscosity, β is the thermal expansion coefficient, g the gravitational acceleration, T the temperature and α the temperature diffusivity. A constant volume flow rate is maintained by the forcing term $\Pi = u_\tau^2/\delta$, where u_τ is the friction velocity and δ the half-channel height. In order to represent structured surfaces an external volume forcing term $F_{IBM,i}$ is introduced by an immersed boundary method (IBM). In the temperature equation the source term Q_{IBM} represents the forcing term to maintain a constant temperature at the surface. The structured surface of the present flow configuration consists of streamwise-aligned ridges on both walls, as shown in figure 2. Due to the presence of these ridges, the half-channel height δ reduces to the effective half-channel height $\delta_{eff} = \delta - \langle \overline{h}_s \rangle$, where $\langle \overline{h}_s \rangle$ is the horizontally averaged mean height of the surface elevation of one wall.

In the case of spanwise heterogeneous surfaces, where the spanwise direction is no longer statistically homogeneous, it is a common choice to decompose the velocity field into its temporal and streamwise mean $\overline{u}_i$ and related random fluctuation u_i'' given by

$$u_i(x, y, z, t) = \overline{u}_i(y, z) + u_i''(x, y, z, t). \tag{2.4}$$

The mean velocity can be further decomposed into its global mean $\langle \overline{u}_i \rangle$, obtained through additional spanwise averaging indicated by angular brackets $\langle \cdot \rangle$, and its coherent or dispersive component $\tilde{u}_i$, which is the spatial fluctuation about $\langle \overline{u}_i \rangle$, and is defined as

$$\overline{u}_i(y, z) = \langle \overline{u}_i \rangle(y) + \tilde{u}_i(y, z). \tag{2.5}$$

The sum of coherent and random fluctuations is defined as fluctuation u_i' such that

$$u_i(x, y, z, t) = \langle \overline{u}_i \rangle(y) + \tilde{u}_i(y, z) + u_i''(x, y, z, t) \tag{2.6}$$

$$= \langle \overline{u}_i \rangle(y) + u_i'(x, y, z, t). \tag{2.7}$$

In this study, the spatial averages are based on intrinsic averaging. This procedure excludes the values at the grid points inside the immersed (solid) body, while the values on the surface are included in the integration. In consequence, the average is computed through normalisation with the fluid area only. This affects the evaluation of global quantities, which are integrated in time and all three spatial directions and are defined as

$$\Phi = \frac{1}{2\delta_{eff} L_z} \int_0^{L_z} \int_{y_b(z)}^{y_t(z)} \bar{\phi} \, \mathrm{d}y \, \mathrm{d}z, \tag{2.8}$$

where ϕ represents an arbitrary quantity and Φ is its volume and time average, while $y_b(z)$ and $y_t(z)$ are the wall-normal surface elevation at the bottom and top walls, respectively.

Note, that this definition applies intrinsic averaging through its spanwise dependent wall-normal integration borders.

The considered flow is characterised by three non-dimensional numbers, namely the Prandtl number Pr, which is the ratio of momentum and thermal diffusivity, the bulk Reynolds number Re_b, describing the ratio of inertial and viscous effects, and the Rayleigh number Ra, characterising the ratio of buoyant and viscous effects, and their definitions are given by

$$Pr = \frac{\nu}{\alpha}, \quad Re_b = \frac{u_b \delta_{eff}}{\nu}, \quad Ra = \frac{(2\delta_{eff})^3 \beta g \Delta T}{\alpha \nu}. \tag{2.9a–c}$$

The bulk velocity is defined as $u_b = 1/(2\delta_{eff} L_z) \int_0^{L_z} \int_{y_b(z)}^{y_t(z)} \bar{u} \, \mathrm{d}y \, \mathrm{d}z$. Here, ΔT is the imposed and constant temperature difference between the bottom and top wall surfaces $\Delta T = T_b - T_t$. The Prandtl number is set to $Pr = 1$ for all considered cases. Following the work by Pirozzoli *et al.* (2017), the bulk Richardson number is defined as

$$Ri_b = \frac{2\delta_{eff} \beta g \Delta T}{u_b^2} = \frac{Ra}{4 Re_b^2 Pr}, \tag{2.10}$$

to characterise the relative importance of buoyancy and inertial effects. Please note that positive values of Ri_b indicate convectively unstable conditions, while in atmospheric flows positive values commonly indicate convectively stable conditions (Wyngaard 2010). Another quantity widely used in the ABL community to categorise the flow is the ratio of the boundary layer depth z_i and the Obukhov length L, which is known as the stability parameter $-z_i/L$ (Wyngaard 2010). For the present channel flow configuration with ridges, this translates into the ratio of δ_{eff} and L, with $L = -u_\tau^3/(\kappa Q \beta g)$, where κ is the von Kármán constant with $\kappa = 0.4$ (Wyngaard 2010), while u_τ and Q are the friction velocity and the vertical heat flux, respectively (both defined in the next paragraph).

The drag exerted on the flow is quantified by the skin friction coefficient C_f and friction Reynolds number Re_τ, which are defined as $C_f = 2u_\tau^2/u_b^2$ and $Re_\tau = u_\tau \delta_{eff}/\nu$, with the friction velocity $u_\tau = (\tau_w/\rho)^{0.5}$ and the wall-shear stress τ_w. The wall-shear stress is determined by extrapolating the total shear stress from the bulk region ($0.5 \leq y/\delta \leq 1.5$) to the virtual wall location $y_0 = \delta - \delta_{eff}$ (Chan-Braun, García-Villalba & Uhlmann 2011). The heat transfer of the flow is characterised by the Nusselt number $Nu = 2\delta_{eff} Q/(\alpha \Delta T)$, with the vertical heat flux Q determined by evaluating the time and horizontally averaged temperature transport equation at the half-channel height $Q = \langle \overline{v'T'} \rangle|_\delta - \alpha \partial \langle \bar{T} \rangle / \partial y|_\delta$ (Stroh *et al.* 2020*a*).

The turbulence level is quantified in this study by the Reynolds number $Re_k = \sqrt{K}\delta_{eff}/\nu$, where K corresponds to the time- and volume-averaged turbulent kinetic energy. This quantity is computed by applying the averaging procedure given in (2.8) $k = 0.5 \cdot \overline{u_i' u_i'}$. A characteristic velocity scale for natural convection is the free-fall velocity $v_f = (2\delta_{eff} \beta g \Delta T)^{1/2}$ and together with the effective channel height the free-fall time t_f can be defined $t_f = 2\delta_{eff}/v_f = (2\delta_{eff}/(\beta g \Delta T))^{1/2}$. The time scale characterising the forced convection processes is the bulk time unit $t_b = \delta_{eff}/u_b$. From the given definitions, the ratio of t_b and t_f results in the following relationship: $t_b/t_f = \sqrt{Ri_b}/2$.

The spanwise height distribution of the streamwise-aligned ridges follows a Gaussian distribution for each individual ridge, which is defined by

$$h_{Gauss}(z) = \sum_{i=1}^{n_g} h_g \exp(-(z - z_{c,i})^2/(2\sigma^2)), \tag{2.11}$$

where n_g is the total number of Gaussian ridges at one wall, h_g is the maximum height of a single Gaussian ridge and $z_{c,i}$ is the spanwise centre position of each individual ridge, given by $z_{c,i} = S\ (i + 0.5)$ with S as the spanwise spacing between two Gaussian ridges. The parameter σ represents the spanwise extent of an individual Gaussian ridge. In this study, the parameters of the Gaussian ridges are set to $h_g = 0.1\delta$ and $\sigma = 0.05\delta$. The cross-sectional area occupied by a single ridge is given by $A_{Gauss} = \sqrt{2\pi} h_g \sigma$. Thus, the effective half-channel height is given by $\delta_{eff} = \delta - \delta_{melt}$ with the melt-down height $\delta_{melt} = n_g A_{Gauss}/L_z$.

The governing equations are numerically solved using direct numerical simulations by means of the open-source code Xcompact3d (Laizet & Lamballais 2009; Bartholomew *et al.* 2020) based on compact finite differences of sixth order and a third-order Runge–Kutta time integration scheme. The representation of the structured surfaces is achieved using an IBM based on polynomial reconstruction of the velocity and temperature fields inside the solid region of the ridges (Gautier, Laizet & Lamballais 2014). The existing code was extended for the simulation of buoyancy effects and the code was validated with the data base for mixed convection and Rayleigh–Bénard flows of Pirozzoli *et al.* (2017), as documented in Appendix A. The simulations were performed on a domain size $L_x \times L_y \times L_z = 16\delta \times 2\delta \times 8\delta$, which is in agreement with Pirozzoli *et al.* (2017), who reported for this domain size insensitivity of the mean velocity and temperature profiles.

2.2. *Cases*

The transition between forced convection structures and streamwise rolls as well as the transition between streamwise rolls and convective cells in mixed convection flows is controlled by the mean shear and buoyancy forcing, which are determined by the imposition of the Reynolds Re_b and Rayleigh number Ra. There are several possibilities which may be used to vary these two dimensionless numbers to achieve the same Richardson number Ri_b, as depicted by the black solid and dashed lines in figure 3(*a*). The simplest approach is to fix one of the dimensionless numbers, while varying the other one and *vice versa*. In the study of Pirozzoli *et al.* (2017), a smooth-wall channel flow is explored for a large parameter space of Re_b and Ra, covering all flow regimes, which is shown in terms of the resulting Nu in figure 3(*b*). For fixed Ra, the initial reduction of Nu with increasing Re_b is associated with the emergence of streamwise rolls, which reduce the effective heat exchange of the convective plumes from the natural convection case. For larger values of Re_b the flow transitions to the forced convection regime where Nu increases with increasing Re_b.

In the current study the spanwise spacing of the Gaussian ridges S is varied in the range of $S/\delta = 0.5, 1, 2, 4, \infty$, where $S = \infty$ corresponds to the smooth-wall case. This translates into an effective half-channel height of $\delta_{eff}/\delta = 0.975, 0.987, 0.994, 0.997$ for the four ridge cases, respectively. Furthermore, the bulk Richardson number Ri_b is varied in such a way as to cover the different flow regimes of mixed convection and their transition ranges. The variation of Ri_b is achieved by two parameter sweeps, one at constant $Ra = 10^7$

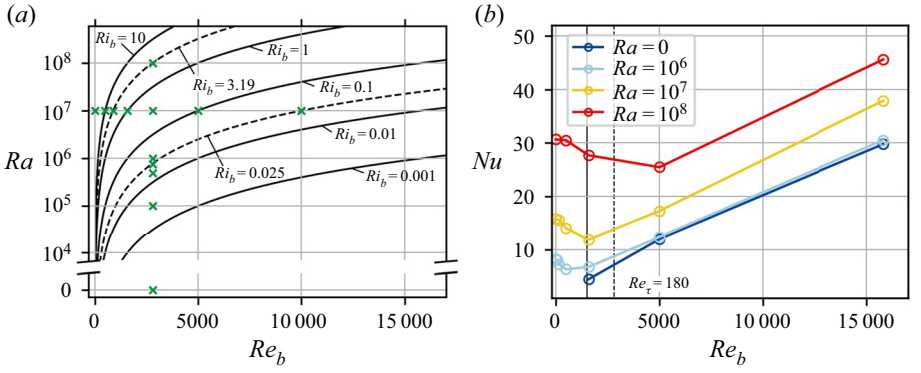

Figure 3. Parameter space of Rayleigh Ra and bulk Reynolds number Re_b in (a). The green marks in (a) indicate the flow parameters of the present simulations and solid and dashed black lines represent isolevels with constant Ri_b. The dashed lines highlight Ri_b values, for which Re-effects are investigated. The Nusselt number Nu over bulk Reynolds number Re_b of the turbulent mixed convection channel flow from Pirozzoli *et al.* (2017) for various Rayleigh numbers is shown in (b). The vertical solid black line separates the transitional and turbulent range for pure forced convection flows.

and varying Re_b and the other sweep for changing Ra at constant $Re_b = 2800$. These two parameter sweeps for the simulations of the present study are represented in figure 3(a) with green crosses, which results in a total number of 65 direct numerical simulations. These two parameter sweeps intersect in the vicinity of the minimum of Nu for $Ra = 10^7$ shown in figure 3(b), which allows us to study the parameter sensitivity of the transition processes from two sides. The two black dashed lines in figure 3(a) indicate isolines of constant Ri_b at which the two transition ranges of mixed convection occur. As will be shown later, the lower isoline $Ri_b = 0.025$ lies within the transition range of forced convection structures to streamwise rolls, while the upper isoline $Ri_b = 3.19$ is in the transition range between streamwise rolls to convective cells. For the present simulations two parameter points with similar Ri_b exist within the two transition ranges, allowing us to study the effect of Re on the flow organisation.

From forced convection flows it is known that the strongest secondary motion occurs for $S/\delta \approx O(1)$ with a spanwise extent of $\approx \delta$ (Vanderwel *et al.* 2019). Since secondary motions of Prandtl's second kind occur only in turbulent flows, the parameter sweep with fixed $Re_b = 2800$ will accommodate these secondary motions for all Ra, which will allow us to study the effect of buoyancy on the secondary motions as well. In the case of the Ra-sweep, this will partly be the case. The spanwise extent of the convection cells and streamwise rolls found in Pirozzoli *et al.* (2017) are roughly 4δ, such that the chosen values of S cover the width of the different aforementioned flow structures.

The grid resolutions for the simulations are chosen according to those used by Pirozzoli *et al.* (2017) for a second-order finite difference code. The grid requirements for mixed convection simulations in conjunction with Gaussian ridges represented by an IBM were investigated in a resolution study presented in Appendix B. It is found that the present grid resolution for smooth-wall mixed convection cases at $Ra = 10^7$ is sufficient for the representation of streamwise Gaussian ridges and a further increase of the resolution results in no significant differences of the mean quantities and profiles. Only for lower Ra does the spanwise grid resolution need to be slightly increased to achieve grid-independent statistical results for the streamwise-aligned ridge cases. The statistical time integration is carried out over at least $1500t_b$ for cases $Ri_b \leq 0.32$, except for the high Re_b cases with

$Ri_b = 0.025$ with time integration of at least $300t_b$. For cases with $Ri_b \geq 1.0$ the time integration comprises at least $400t_f$, while the high Ra cases with $Ri_b = 3.2$ and $Ra = 10^8$ were averaged over at least $120t_f$.

3. Results

3.1. *Global flow properties*

The results of the global flow properties for the different simulations are presented in table 1, where the configurations are arranged according to the parameter triad (Ra, Re_b, S/δ). The smooth-wall configurations are indicated by $S = \infty$ and the configurations with streamwise-aligned ridges are listed with decreasing S. Since the forced and mixed convection cases are run at constant flow rate, the presence of the Gaussian ridges will increase the drag, which translates into an increase of C_f and Re_τ compared with the respective case with smooth-wall conditions. As can be seen for all considered cases, the steady decrease of S leads to a monotonic increase of C_f and Re_τ compared with the smooth-wall case. For forced convection the increase of C_f is up to 26 %, while the largest increase is found for $Ri_b = 10$ with 45 %. Due to the changing friction drag, the ridge height in wall units h_g^+ changes for all cases as well, and is in the range $7 \leq h_g^+ \leq 60$ for the current configurations. In the case of pure forced convection, turbulent secondary motions induced by streamwise-aligned ridges are known to increase the global friction as well as the heat transfer of the flow compared with smooth-wall conditions (Stroh *et al.* 2020*a*). This behaviour is also observed for the present forced convection case with streamwise-aligned Gaussian ridges, where for the densest ridge spacing $S = 0.5\delta$ the heat transfer increases 16 % compared with the smooth-wall case. In a similar range 17 % is the increase for the natural convection case, and the largest increase is found for $Ri_b = 3.2$ with 32 %.

While the skin friction drag increases with decreasing S and increasing wetted surface area, this behaviour is not found for the heat transfer for all present cases. This is illustrated for the two parameter sweeps at constant $Re_b = 2800$ in figure 4(*a*) and at constant $Ra = 10^7$ in figure 4(*b*). The forced convection case $Ra = 0$ and weak convective case $Ra = 10^5$ in figure 4(*a*) show the successive increase of Nu with decreasing ridge spacing S. An increase of Ra or Ri_b introduces an additional buoyant contribution to the vertical mixing, resulting in larger heat transfer and for large Rayleigh numbers ($Ra > 10^6$), which represent configurations where buoyancy is comparable to shear or even stronger, the monotonic increase of Nu with decreasing S is also found. However, for the particular cases $Ra = 7.5 \times 10^5$ ($Ri_b = 0.024$) and $Ra = 10^6$ ($Ri_b = 0.032$) heat transfer does not monotonically increase with decreasing S, which is visible in the inset of figure 4(*a*).

In figure 4(*b*) the natural convection case is given by $Re_b = 0$ and the influence of buoyancy is successively reduced by increasing Re_b. The minimum found for Nu is associated with the break up of the thermal plumes of the Rayleigh–Bénard case, when shear is added, and has been reported for unstable thermal stratification in Poiseuille and Couette flows (Scagliarini, Gylfason & Toschi 2014; Blass *et al.* 2020). The non-monotonic behaviour of Nu with decreasing S seen in figure 4(*a*) also occurs for the largest $Re_b = 10\,000$ case ($Ri_b = 0.025$), which is in a similar bulk Richardson number range to the former cases. Thus, all cases which depict a non-monotonic behaviour of Nu with respect to S fall within a range of bulk Richardson values $Ri_b = 0.016$–0.032, where shear effects are strong and buoyancy effects are weak. It will be shown that this range of Richardson numbers marks the transition from forced convection structures to streamwise rolls and the ridge spacing S affects and alters this transition.

Ra	Re_b	Ri_b	S/δ	$N_x \times N_y \times N_z$	Re_τ	Re_k	$C_f (\times 10^{-3})$	Nu	$-\delta_{eff}/L$
0	2800	0	∞	$512 \times 193 \times 384$	178.5	228.1	8.1	7.4	—
0	2800	0	4	$512 \times 193 \times 384$	180.0	236.9	8.3	7.5	—
0	2800	0	2	$512 \times 193 \times 384$	181.7	244.1	8.5	7.7	—
0	2800	0	1	$512 \times 193 \times 384$	184.2	250.8	8.8	8.0	—
0	2800	0	0.5	$512 \times 193 \times 384$	196.3	258.5	10.2	8.6	—
10^5	2800	0.003	∞	$512 \times 193 \times 256$	179.3	229.1	8.2	7.5	0.003
10^5	2800	0.003	4	$512 \times 193 \times 384$	180.4	238.3	8.3	7.7	0.003
10^5	2800	0.003	2	$512 \times 193 \times 384$	182.0	244.7	8.5	7.8	0.003
10^5	2800	0.003	1	$512 \times 193 \times 384$	184.7	251.2	8.9	8.1	0.003
10^5	2800	0.003	0.5	$512 \times 193 \times 384$	196.7	259.1	10.2	8.6	0.003
5.0×10^5	2800	0.016	∞	$512 \times 193 \times 256$	180.5	234.3	8.3	8.1	0.017
5.0×10^5	2800	0.016	4	$512 \times 193 \times 384$	181.8	240.9	8.5	8.1	0.017
5.0×10^5	2800	0.016	2	$512 \times 193 \times 384$	183.2	247.3	8.6	8.2	0.017
5.0×10^5	2800	0.016	1	$512 \times 193 \times 384$	186.1	253.0	9.0	8.4	0.016
5.0×10^5	2800	0.016	0.5	$512 \times 193 \times 384$	198.1	261.1	10.4	9.0	0.014
7.5×10^5	2800	0.024	∞	$512 \times 193 \times 256$	180.4	249.1	8.3	9.4	0.030
7.5×10^5	2800	0.024	4	$512 \times 193 \times 384$	181.8	249.5	8.5	9.2	0.029
7.5×10^5	2800	0.024	2	$512 \times 193 \times 384$	183.6	252.2	8.7	9.1	0.028
7.5×10^5	2800	0.024	1	$512 \times 193 \times 384$	187.0	254.1	9.1	8.6	0.025
7.5×10^5	2800	0.024	0.5	$512 \times 193 \times 384$	199.4	262.7	10.5	9.2	0.022
10^6	2800	0.032	∞	$512 \times 193 \times 256$	178.9	257.1	8.2	9.7	0.042
10^6	2800	0.032	4	$512 \times 193 \times 384$	180.9	256.7	8.4	9.7	0.041
10^6	2800	0.032	2	$512 \times 193 \times 384$	183.2	261.1	8.6	9.8	0.040
10^6	2800	0.032	1	$512 \times 193 \times 384$	186.8	261.4	9.1	9.6	0.037
10^6	2800	0.032	0.5	$512 \times 193 \times 384$	198.9	266.2	10.5	10.0	0.032
10^7	0	∞	∞	$1024 \times 257 \times 512$	—	237.2	—	15.7	∞
10^7	0	∞	4	$1024 \times 257 \times 512$	—	236.9	—	16.0	∞
10^7	0	∞	2	$1024 \times 257 \times 512$	—	236.7	—	16.3	∞
10^7	0	∞	1	$1024 \times 257 \times 512$	—	238.9	—	16.9	∞
10^7	0	∞	0.5	$1024 \times 257 \times 512$	—	245.7	—	18.4	∞
10^7	500	10.0	∞	$1024 \times 257 \times 512$	71.0	250.0	40.3	13.9	9.743
10^7	500	10.0	4	$1024 \times 257 \times 512$	72.1	243.7	41.8	14.2	9.461
10^7	500	10.0	2	$1024 \times 257 \times 512$	73.2	239.9	43.2	14.4	9.213
10^7	500	10.0	1	$1024 \times 257 \times 512$	77.5	226.9	48.8	15.1	8.122
10^7	500	10.0	0.5	$1024 \times 257 \times 512$	83.9	235.7	58.4	17.2	7.275
10^7	885	3.19	∞	$1024 \times 257 \times 512$	97.7	263.4	24.4	12.6	3.373
10^7	885	3.19	4	$1024 \times 257 \times 512$	99.3	262.5	25.2	12.9	3.300
10^7	885	3.19	2	$1024 \times 257 \times 512$	101.0	252.5	26.2	13.1	3.174
10^7	885	3.19	1	$1024 \times 257 \times 512$	105.5	240.0	28.9	13.6	2.903
10^7	885	3.19	0	$1024 \times 257 \times 512$	111.7	236.1	33.0	15.2	2.729
10^7	1581	1.0	∞	$1024 \times 257 \times 512$	134.2	304.1	14.4	11.9	1.231
10^7	1581	1.0	8	$1024 \times 257 \times 512$	135.2	300.6	14.7	12.0	1.210
10^7	1581	1.0	4	$1024 \times 257 \times 512$	136.7	300.2	15.0	12.1	1.184
10^7	1581	1.0	2	$1024 \times 257 \times 512$	138.9	285.6	15.6	12.2	1.140
10^7	1581	1.0	1	$1024 \times 257 \times 512$	143.1	278.5	16.7	12.6	1.072
10^7	1581	1.0	0.5	$1024 \times 257 \times 512$	152.5	275.2	19.3	13.9	0.979

Table 1. For caption see on next page.

Ra	Re_b	Ri_b	S/δ	$N_x \times N_y \times N_z$	Re_τ	Re_k	$C_f(\times 10^{-3})$	Nu	$-\delta_{eff}/L$
10^7	2800	0.32	∞	$1024 \times 257 \times 512$	190.4	353.2	9.3	12.3	0.446
10^7	2800	0.32	4	$1024 \times 257 \times 512$	193.9	350.6	9.6	12.7	0.434
10^7	2800	0.32	2	$1024 \times 257 \times 512$	198.1	352.8	10.1	13.1	0.422
10^7	2800	0.32	1	$1024 \times 257 \times 512$	204.9	348.8	10.9	13.8	0.401
10^7	2800	0.32	0.5	$1024 \times 257 \times 512$	216.2	349.8	12.4	15.1	0.373
10^7	5000	0.1	∞	$1024 \times 257 \times 512$	304.5	499.1	7.4	17.1	0.152
10^7	5000	0.1	4	$1024 \times 257 \times 512$	306.4	497.0	7.5	17.3	0.150
10^7	5000	0.1	2	$1024 \times 257 \times 512$	311.4	501.7	7.8	17.7	0.146
10^7	5000	0.1	1	$1024 \times 257 \times 512$	316.9	499.9	8.2	18.2	0.143
10^7	5000	0.1	1	$1024 \times 257 \times 512$	328.9	504.0	8.9	19.3	0.135
10^7	10 000	0.025	∞	$1536 \times 513 \times 1024$	552.2	847.6	6.1	28.4	0.042
10^7	10 000	0.025	4	$1536 \times 513 \times 1024$	555.0	822.7	6.2	28.1	0.041
10^7	10 000	0.025	2	$1536 \times 513 \times 1024$	558.3	841.3	6.3	28.4	0.041
10^7	10 000	0.025	1	$1536 \times 513 \times 1024$	570.5	825.5	6.6	28.1	0.038
10^7	10 000	0.025	0.5	$1536 \times 513 \times 1024$	585.2	831.9	7.0	27.1	0.034
10^8	2800	3.19	∞	$2048 \times 513 \times 1024$	246.1	749.3	15.5	25.6	4.297
10^8	2800	3.19	4	$2048 \times 513 \times 1024$	249.5	791.9	15.9	26.9	4.327
10^8	2800	3.19	2	$2048 \times 513 \times 1024$	259.3	718.1	17.3	27.6	3.964
10^8	2800	3.19	1	$2048 \times 513 \times 1024$	269.3	695.1	18.7	29.4	3.761
10^8	2800	3.19	0.5	$2048 \times 513 \times 1024$	295.1	710.6	22.8	33.7	3.277

Table 1. List of simulation configurations with flow parameters and resulting global flow properties.

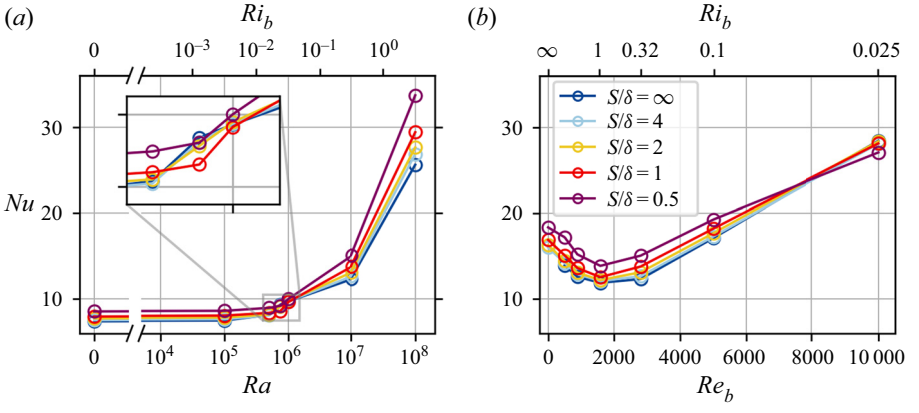

Figure 4. Nusselt number Nu as a function of Rayleigh number Ra in (a) and bulk Reynolds number Re_b in (b) for different ridge spacings S. In (a) the bulk Reynolds number $Re_b = 2800$ and in (b) the Rayleigh number $Ra = 10^7$ is kept constant.

In the case of mixed convection, turbulence is driven by two generation mechanisms, the production by shear and by buoyancy, and the exact turbulence level cannot be inferred *a priori* by Ra and Re_b. The same holds for the bulk Richardson number Ri_b. To rule out effects caused by the different turbulence levels or Reynolds number effects, which will be discussed in § 3.6, we separate those cases with significantly higher turbulence levels from the cases with comparable values. For the subsequent discussion and sections only cases which fall in a range of Reynolds number values $Re_k = 200$–355 are considered.

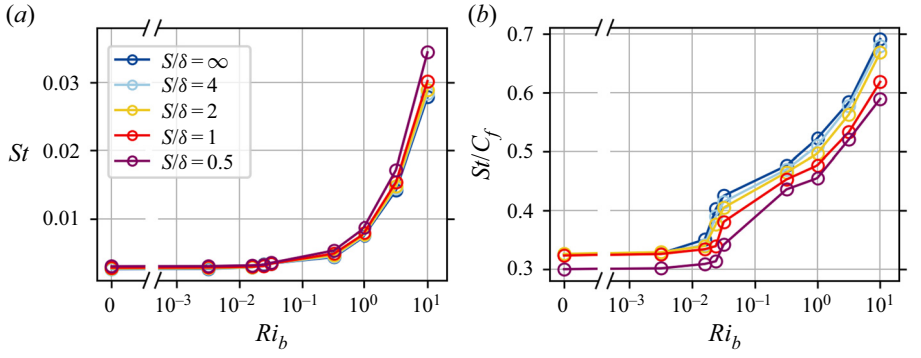

Figure 5. Stanton number St in (a) and ratio of St to C_f in (b) as a function of bulk Richardson number Ri_b for different ridge spacings S. The selected cases have values of the Reynolds number Re_k in a similar range.

This selection includes only those cases of the two parameter sweeps for which $Ra \leq 10^7$ and $Re_b \leq 2800$. Instead of using the pairs of Ra and Re_b, the bulk Richardson number Ri_b is used in the following to characterise the relative importance of buoyancy and shear effects. In analogy to $Ri = Ra/(4Re_b^2 Pr)$, Nu is replaced by the Stanton number $St = Nu/(Re_b Pr)$. The corresponding results are presented in figure 5(a) and reveal an increase of St with Ri_b.

The relative increase between heat and momentum transfer is characterised by the ratio St/C_f, which is shown in figure 5(b). For each S it can be seen that larger values of Ri_b induce larger St/C_f values. This implies that buoyancy effects lead to a larger increase of heat transfer than of momentum transfer. In addition, a consistent influence of the ridges can be observed in this representation. A decrease of S results in lower St/C_f for all Ri_b. This is also reflected in the stability parameter $-\delta_{eff}/L$ in table 1, which is another quantity to compare the relative heat and momentum transfer. The most distinct property of figure 5(b) is the strong increase of St/C_f in the range $Ri_b = 0.016$–0.032. This increase is delayed to larger Ri_b with decreasing S and can be linked to a reorganisation of the turbulent flow structures, as discussed in the following section.

3.2. *Turbulent flow structures*

The different flow organisations of mixed convection flows observed over smooth-wall conditions can be visualised by instantaneous velocity or temperature fluctuations in horizontal planes (Salesky *et al.* 2017). The influence of heterogeneous surfaces on this flow organisation is shown for various pairs of Ri_b and S for the instantaneous temperature fluctuations in wall-parallel planes located at the half-channel height ($y = \delta$) in figure 6 and slightly above the top of the ridges ($y = 0.15\delta$) in figure 7. Please note that the discussion for the near-wall region refers to the bottom wall, unless stated otherwise. Both horizontal planes display the same instantaneous realisation of the flow field and comprise cases that fall into a similar range of turbulent Reynolds number Re_k. The Ri_b increases from top to bottom, starting with the forced convection case $Ri_b = 0$ ($Re_b = 2800$, $Ra = 0$) in the top panel and the natural convection case $Ri_b = \infty$ ($Re_b = 0$, $Ra = 10^7$) in the bottom panel. The ridge spacing S/δ decreases from left to right, with the smooth-wall case displayed in the first column of figures 6 and 7.

Considering the smooth-wall cases $S = \infty$ first, the flow topology of the forced convection case has a spotty organisation which is also the case for the mild convective

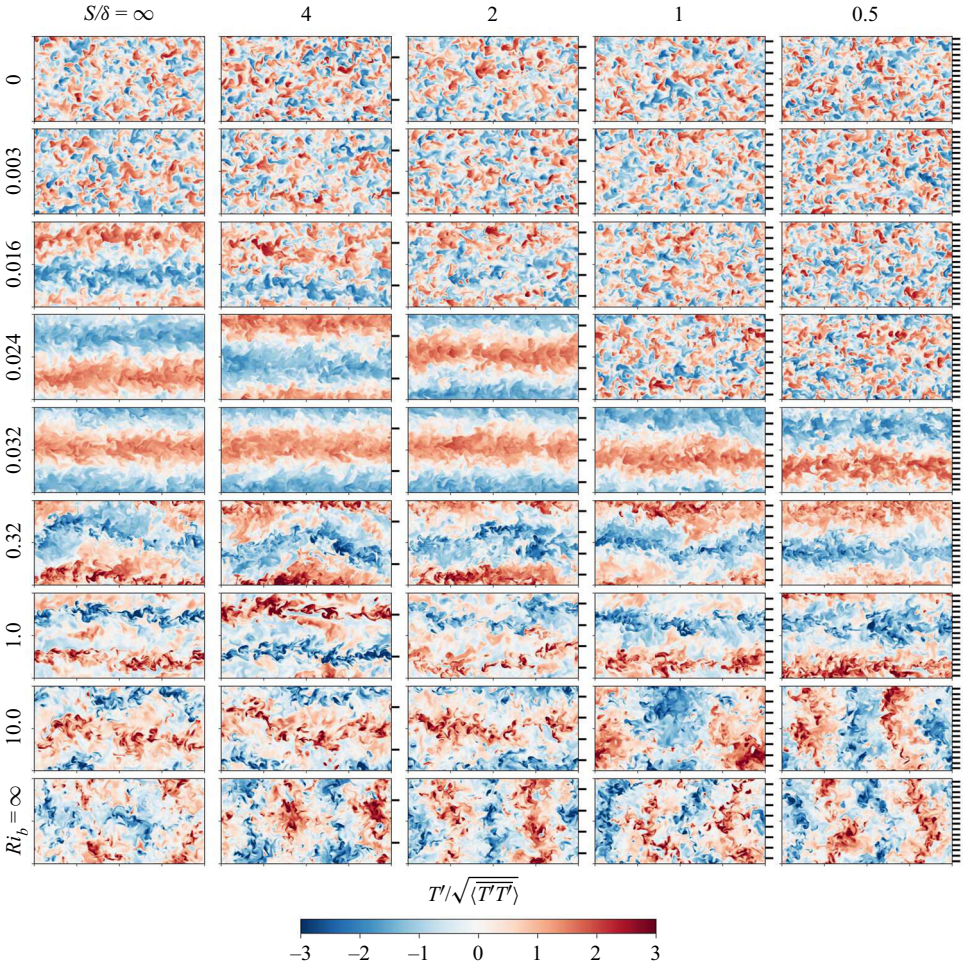

Figure 6. Instantaneous temperature fluctuation fields at the half-channel height position $y = \delta$ for varying Richardson number Ri_b and different spanwise spacings S of the Gaussian ridges. The spanwise position of the ridges is indicated by the black lines on the right outer frame of the figures. The horizontal sections show the full simulation domain of size $16\delta \times 8\delta$.

case $Ri_b = 0.003$ ($Re_b = 2800$, $Ra = 10^5$) in figure 6. The transition to streamwise rolls takes place for slightly larger buoyant forcing for case $Ri_b = 0.016$ ($Re_b = 2800$, $Ra = 5 \times 10^5$), but the rolls still display some patchiness. This transition also results in a change of the near-wall structures as can be seen in figure 7, where strong elongated temperature fluctuations are preferentially located in regions of streamwise roll updrafts, and are less pronounced in the downdraft region. These elongated temperature fluctuations coincide with the near-wall low-speed streaks (not shown here), since for neutral and moderately convective cases the temperature behaves like a passive scalar with strong correlation with the streamwise velocity (Khanna & Brasseur 1998). The formation mechanism of streamwise rolls is strongly linked to localised buoyancy forces, which concentrate in low-speed streaks and thereby create linear updrafts (Khanna & Brasseur 1998). Multiple updrafts can merge to a strong buoyancy-enhanced streak, forming the updraft region of the streamwise roll in figure 6. This updraft reaches the opposing wall and reduces or

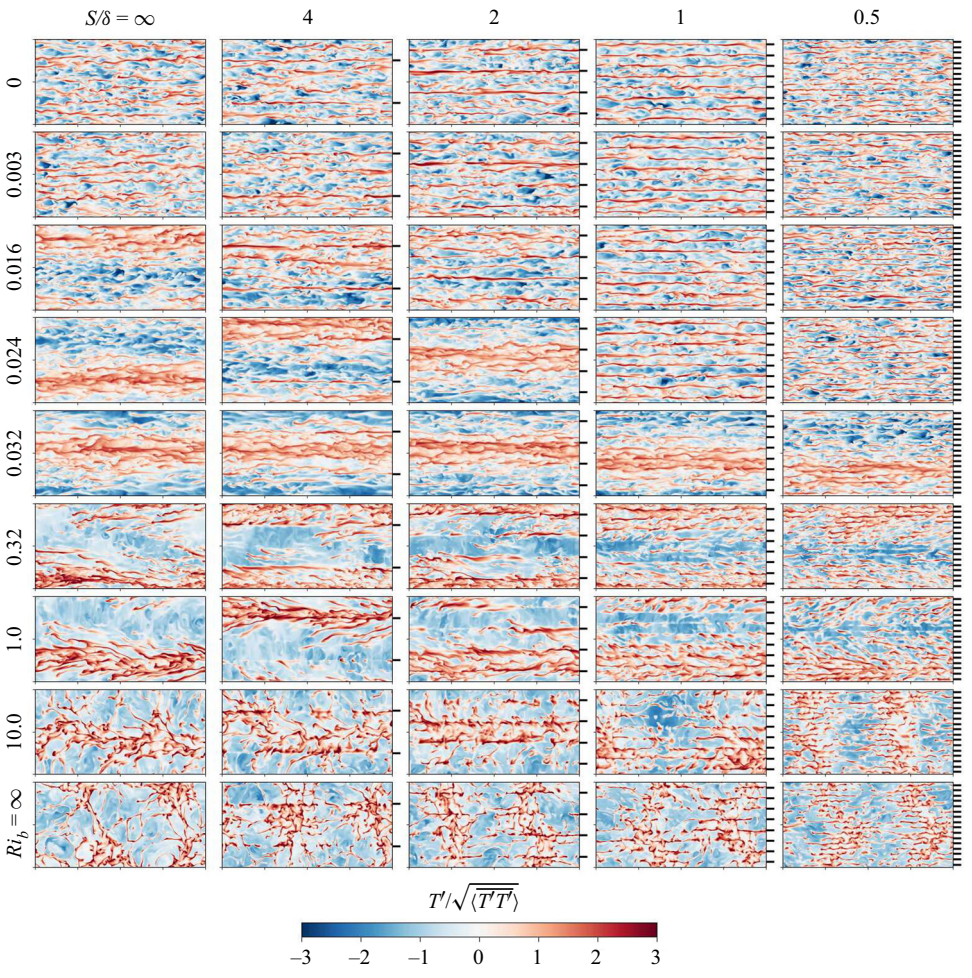

Figure 7. Instantaneous temperature fluctuation fields at $y = 0.15\delta$ for varying Richardson number Ri_b and different spanwise spacing S of the Gaussian ridges.

destroys the coherence of the low-speed streaks there. At the same time, between these impingement regions of the updrafts at the opposite wall, buoyancy-enhanced low-speed streaks can form, which in turn generate a strong localised downdraft and in combination with the updrafts result in a large-scale streamwise roll motion in the cross-section.

In contrast to case $Ri_b = 0.016$, the streamwise roll of case $Ri_b = 0.024$ in figure 6 is more articulated in its structure, which is associated with a sudden increase of St/C_f in figure 5(*b*). The streamwise rolls persist up to $Ri_b = 1$ in figure 6 with a spanwise wavelength of approximately 8δ, such that the chosen domain size is able to accommodate a single pair of counter-rotating rolls as reported by Pirozzoli *et al.* (2017). For the cases $Ri_b = 0.32$ and $Ri_b = 1.0$ in figure 6 the rolls show a strong waviness of the thermal up- and downdrafts, which is also seen in the near-wall region where the updraft region encompasses spanwise inclined near-wall streaks in figure 7. When buoyancy forces become more important, the streamwise roll is more disrupted and reduce its streamwise coherence, since thermal plumes become dynamically more important (see case $Ri_b = 10$ in figure 6) (Salesky *et al.* 2017). The increased influence of buoyancy also modifies the near-wall structures, where cell-like structures appear in the updraft region, which still

depict some streamwise coherence, as seen in figure 7. For the Rayleigh–Bénard case $Ri_b = \infty$ ($Re_b = 0$, $Ra = 10^7$) in figure 6, the streamwise roll is not present any more and the flow organises into convective cells. These structures have a preferential roll orientation in the x- and z-directions, also seen in the near-wall region in figure 7, which is due to the rectangular domain size (Pirozzoli *et al.* 2017)

The introduction of the ridges displays no significant differences of the flow structures in the channel centre for the forced convection case $Ri_b = 0$ and weak buoyancy case $Ri_b = 0.003$ compared with the smooth-wall case. However, the elongated high temperature fluctuations in the near-wall region are more coherent in the streamwise direction in the case of ridge spacings $S = \delta, 2\delta, 4\delta$, for which they preferentially occur at the spanwise ridge position. For mild buoyancy effects, these elongated temperature regions collapse with low-speed streaks (not shown here), forming low-momentum pathways directly above the ridges. As such, the preferential position of the low-speed streaks coincides with the mean upward motion of the secondary motions, which will be shown in § 3.3. For the densest ridge spacing $S = 0.5\delta$ these elongated structures still occur at the ridges, however, they appear less coherent in the streamwise direction.

Significant effects of the ridges can be seen for the transition between forced convection structures and streamwise rolls in figure 6 for cases $Ri_b = 0.016$–0.032. As shown before, the transition towards streamwise rolls for smooth-wall conditions takes place at $Ri_b = 0.016$ and this transition can be also observed for the coarsest ridge spacing $S = 4\delta$, which, however, is more interrupted by individual turbulent spots than the smooth-wall case. This is also reflected in a change of the near-wall structures, where, for case $S = 4\delta$, the elongated high temperature fluctuations still favour the updraft region, but in contrast to the smooth-wall case, also occur inside the downdraft region at the ridge position (figure 7). For denser ridge spacing $S < 4\delta$ the preferred concentration of low-speed streaks is not observed anymore. Therefore, the streamwise roll is not visible in the channel core and the flow structures resemble those seen for the forced convection and weak buoyancy cases $Ri_b = 0.003$. For slightly larger bulk Richardson number $Ri_b = 0.024$ the streamwise roll is now clearly visible for the two coarsest ridge spacings $S = 4\delta$ and $S = 2\delta$ in figure 6, and strong enough to reorganise the near-wall structures seen in figure 7, while for the denser ridge spacings the streamwise roll is not present. Eventually, the streamwise roll is observed for all ridge spacings S at $Ri_b = 0.032$, while for the denser ridge spacings still some spot-like structures overlap with the rolls. Considering figure 5(*b*), the delayed transition between forced convection structures and streamwise rolls with decreasing S can be related to the increased drag introduced by the ridges. Denser ridge spacings introduce more drag and shear in the near-wall region, and in consequence larger buoyancy forces are required to form the streamwise rolls which in turn induce an increase in heat transfer.

The streamwise roll, present for the intermediate Richardson number $Ri_b = 0.32$ and $Ri_b = 1.0$ cases (figure 6), displays no significant influence of the ridges. This is likewise the case for the near-wall region in figure 7, where it can be seen that the formation of high temperature fluctuations occur inside the updraft region of the roll.

At higher convective conditions for $Ri_b = 10.0$ the streamwise roll is present for the smooth-wall case and the two coarsest ridge spacings $S = 2\delta, 4\delta$, while it completely disappears for denser ridge spacings $S \leq \delta$. For $S = \delta$ the streamwise roll is replaced by convection cells, resembling that found for the Rayleigh–Bénard case with a spacing of $S = 4\delta$. For the densest ridge spacing $S = 0.5\delta$, rolls with a preferential orientation in the spanwise direction occur, which have similarities to the densest ridge spacing $S = 0.5\delta$ of the Rayleigh–Bénard case. This transition from roll to cell structures is also reflected

in a transition of the near-wall structures in figure 7. The roll-to-cell transition is also observed for the lower bulk Richardson case $Ri_b = 3.2$ (higher Re_k) for the same ridge spacings S (not shown). This result is remarkable, since the transition from roll to cell structures over homogeneous wall conditions in ABL is expected to begin at larger values of the stability parameter $-z_i/L \approx 26$ (Salesky *et al.* 2017), while the stability parameter for the cases $Ri_b = 3.2$ and $Ri_b = 10.0$ are in the range $-\delta_{eff}/L = 3.4$–9.7. This illustrates that streamwise-aligned ridges reduce significantly the range of Ri_b or $-\delta_{eff}/L$ in which streamwise rolls appear. This suggests that heterogeneous rough surfaces can trigger the roll-to-cell transition with smaller buoyancy forces.

As can be seen for the Rayleigh–Bénard case $Ri_b = \infty$ in figure 6, decreasing the ridge spacings S results in an increasingly preferential orientation of the convective cell towards the spanwise direction z. The rolls with orientation in the x-direction experience increasing lateral drag as S decreases, and for $S \leq 2\delta$ these rolls can eventually no longer emerge and only rolls in the z-direction, whose circulation is along the ridge direction, occur. This observation will be discussed further in § 3.4. The increase of Nu for smaller S is also reflected by intensified thermal up- and downdrafts in the channel centre plane. We note that additional simulations for $S = \infty$ and $S = 0.5\delta$ in a wider domain ($L_x = L_z = 16\delta$) do not indicate a domain size dependence of the obtained results.

3.3. *Mean properties*

The effects of ridge spacing S and the relative strength of the shear and buoyancy effects on the time and horizontally averaged mean streamwise velocity and temperature profiles are shown in figure 8. The mean temperature is represented as the difference from the bottom wall temperature T_b and scaled by the friction temperature $T_\tau = Q/\rho c_p u_\tau$. Starting from forced convection, the trend of the mean profiles to become flatter with increasing Ri_b is consistent with the results of Pirozzoli *et al.* (2017). The logarithmic region of $\langle \bar{u} \rangle$ found for a weak convective condition starts to deviate at $Ri_b = 0.032$. The reduction of the spanwise ridge spacing S leads to a decrease of the mean streamwise velocity and temperature profile, which is in agreement with increased surface drag (see table 3 and figure 5*b*). However, temperature profiles within the transition range from forced convection structures to streamwise rolls show deviations from this behaviour close to the channel core, which is highlighted by the inset of figure 8(*b*). In this figure, it can be seen for $Ri_b = 0.024$ and $Ri_b = 0.032$ that the temperature takes larger values with decreasing S at the channel centre and at the same time the slope of the temperature increases. This indicates that the thermal mixing of the flow is increasingly weakened by the ridges. The transition from streamwise rolls to spot-like structures for case $Ri_b = 0.024$ can be also inferred from the similar slope of $S = \delta$ and $S = 0.5\delta$ to that of the forced convection cases. Interestingly, for case $Ri_b = 0.032$, where all S feature streamwise rolls, the slope of the temperature profile for $S = 0.5\delta$ also resembles that of the forced convection cases, which indicates that the transition point is already close. As can be seen, the influence and effects of the ridge spacing S are of the same order as a change of the bulk Richardson number Ri_b.

The occurrence of secondary motions over streamwise-aligned ridges in forced convection flows is observed in time- and streamwise-averaged velocity fields in the channel cross-section, and is shown for case $Ri_b = 0$ in figure 9. The relative strengths of the coherent motion among the different ridge spacings can be directly compared, due to the same scaling of the cross-sectional velocity components in bulk units. The smooth channel flow exhibits no coherent motion in the cross-section (not shown here), while

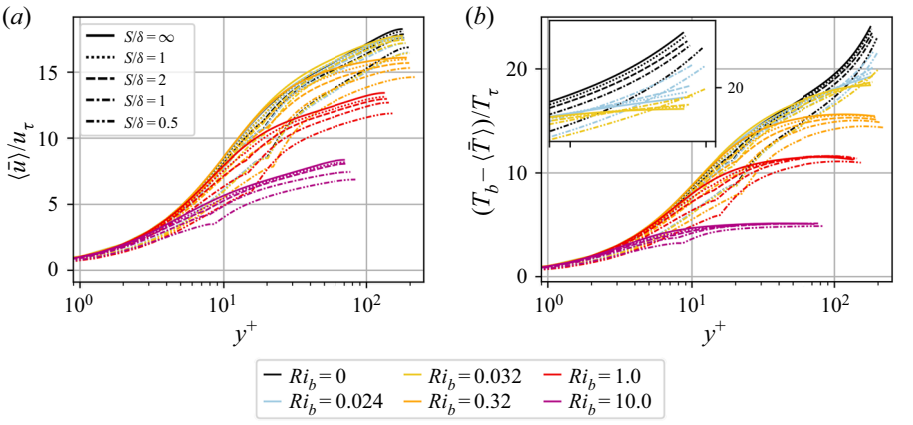

Figure 8. Effect of Richardson number Ri_b and S on wall-normal profiles of streamwise mean velocity and mean temperature for different ridge spacings S scaled in wall units.

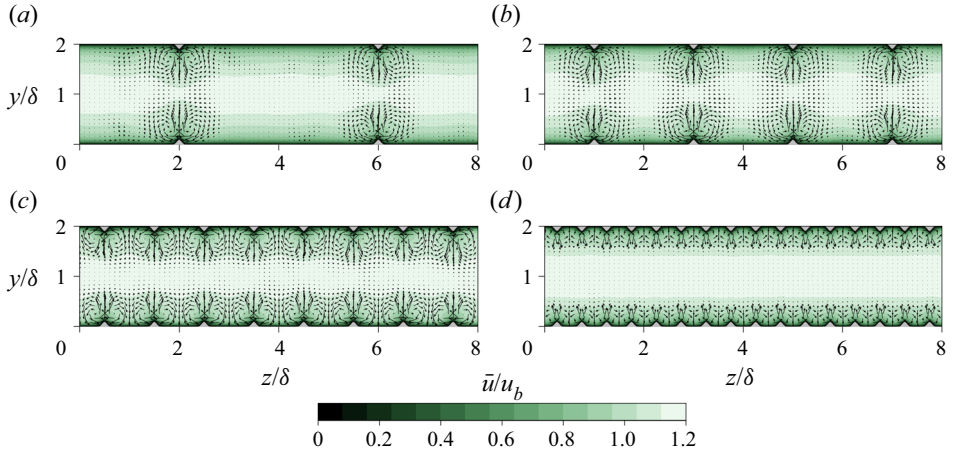

Figure 9. Effect of spanwise spacing on mean streamwise velocity for forced convection case $Ri_b = 0$ ($Re_b = 2800$, $Ra = 0$). The spanwise spacing of the Gaussian ridges is $S = 4\delta$ (*a*), $S = 2\delta$ (*b*), $S = \delta$ (*c*) and $S = 0.5\delta$ (*d*). Arrows indicate cross-sectional velocity components and are scaled by bulk velocity.

for streamwise-aligned ridges the secondary motions appear in the mean flow field as counter-rotating vortices at each ridge in figure 9. These vortices introduce an upward motion above each ridge and a downward motion is located to the side of each ridge. As can be seen, the secondary motion induces a bulging of the mean streamwise velocity above the ridge, transporting low momentum into the bulk region, and for large spacings $S = 4\delta$ and $S = 2\delta$ almost reaching the half-channel height. The spacing between the ridges of case $S = 4\delta$ in figure 9(*a*) is large enough, so that a homogeneous region unaffected by the secondary motion can form between the ridges. Decreasing the spanwise spacing S, the secondary motions fill almost the entire channel domain for case $S = 2\delta$ (figure 9(*b*) and case $S = \delta$ (figure 9(*c*). However, for case $S = \delta$ the wall-normal extent of the secondary motions is slightly reduced compare with case $S = 2\delta$, which indicates that the secondary motions of adjacent ridges affect each other at a spacing of $S = \delta$. Further decrease of the ridge spacing to $S = 0.5\delta$ (figure 9*d*) shows a significant reduction of the spatial extent of the secondary motion in the wall-normal direction.

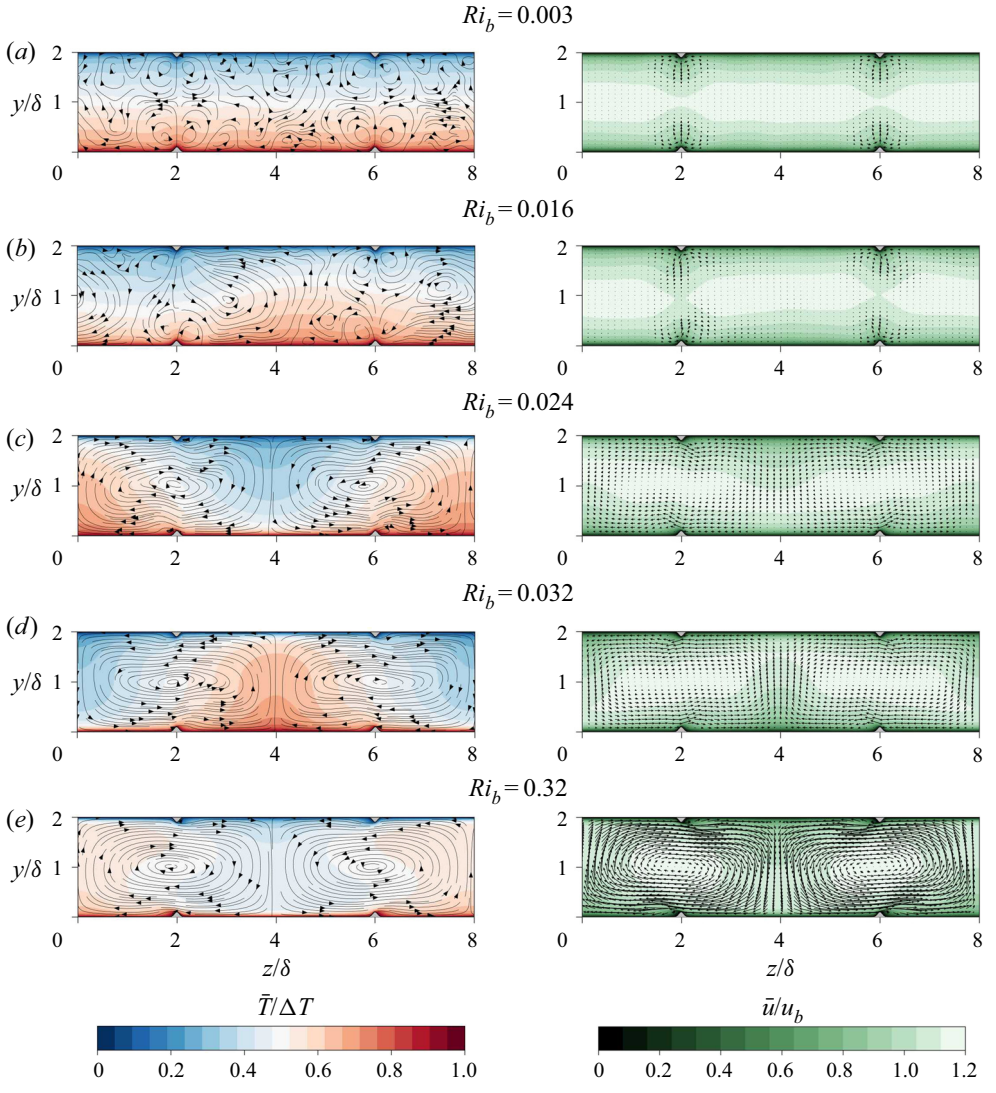

Figure 10. Effect of buoyancy on streamwise mean velocity and temperature for constant $Re_b = 2800$ and $S = 4\delta$ for different Richardson numbers. Arrows indicate cross-sectional velocity components and are scaled by bulk velocity.

The investigation of the horizontal fields of the instantaneous temperature have shown that the transition of the flow topology for smooth-wall conditions is affected by the introduction of the streamwise-aligned ridges. This reorganisation is also reflected in the mean streamwise velocity and temperature fields in the cross-section, which are shown in figure 10 for the transition from forced convection structures to streamwise rolls at a ridge spacing of $S = 4\delta$. The strengths of the cross-sectional velocity components are represented by the arrows in the mean streamwise velocity field, while their flow topology is visualised by streamlines in the mean temperature field. The weak buoyancy case $Ri_b = 0.003$ is shown in figure 10(*a*) and, similar to the forced convection case in figure 9, secondary motions are present in the mean velocity field which also leads to a bulging of the mean temperature at the ridges.

The transition towards streamwise rolls has been seen to occur for smooth-wall conditions at $Ri_b = 0.016$, while for $S = 4\delta$ a slight tendency towards rolls was present. Figure 10(*b*) shows that secondary motions can still occur at the ridges, although two diminished roll structures emerge that extend to the opposite wall. This in turn replaces the local bulging of the mean temperature at the ridge by a significant wider bulging of the mean temperature. As Ri_b increases to $Ri_b = 0.024$ the secondary motions are replaced by a streamwise roll. The upward and downward motions of the convective rolls are located in the valley between two Gaussian ridges and each roll has a spanwise extent of four half-channel heights. As can be seen in the streamwise mean velocity field, the rolls induce a stronger cross-sectional velocity in the entire channel, which introduces a recirculation zone at the leeward side of the Gaussian ridges. The cross-sectional velocities of the streamwise roll further intensify as Ri_b increases, as can be seen for case $Ri_b = 0.32$ in figure 10(*e*).

Figure 11 shows the effect of S on the mean temperature and mean streamwise velocity for case $Ri_b = 10$, which features the transition between streamwise rolls and convective cells. The bulging of $\bar{T}$ and $\bar{u}$ due to the streamwise roll is found for smooth-wall conditions and $S \geq \delta$, while this is not found for the densest ridge spacing $S = 0.5\delta$. For the latter case this reflects the transition from streamwise rolls to convective cells with preferential orientation in the z-direction found in the instantaneous temperature fields in figures 6 and 7, which results in the disappearance of the cross-sectional motion in figure 11(*e*). The up- and downdrafts of the streamwise rolls for $S = 4\delta$ and $S = 2\delta$ are located in the valleys between adjacent ridges. For the former case the lateral movement of the roll encounters the ridge in the middle between up- and downdrafts, where large spanwise velocities of the roll occur. The ridges close to the up- and downdrafts for case $S = 2\delta$ support the wall-normal motion of the roll by the upward deflection at the ridges, which results in stronger bulging of $\bar{u}$ at the up- and downdraft region compared with $S = 4\delta$. As can be seen for case of $S = \delta$ in figure 11(*d*) the strength of the cross-sectional motion is reduced compared with the coarser S cases, since the roll experiences more lateral drag on crossing the ridges due to decreasing S.

3.4. *Turbulent properties*

The mean velocity and temperature fields presented in the previous section have shown that secondary motions and streamwise rolls manifest as large-scale coherent motion in the cross-sectional plane. The energetics of these structures is further analysed by applying the decomposition procedures of (2.6) and (2.7) to the turbulent kinetic energy $k = 0.5\overline{u_i' u_i'}$. This separates the turbulent kinetic energy k into its coherent contribution $\tilde{k}$ and random contribution k'' given by $k = \tilde{k} + k''$. In order to extract the influence of the cross-sectional motion, the coherent turbulent kinetic energy $\tilde{k}$ is decomposed into its cross-sectional $\tilde{k}_c = 0.5(\tilde{v}\tilde{v} + \tilde{w}\tilde{w})$ and streamwise $\tilde{k}_s = 0.5\tilde{u}\tilde{u}$ parts. Since the global mean velocity components $\langle\bar{v}\rangle$ and $\langle\bar{w}\rangle$ are zero, the coherent components $\tilde{v}$ and $\tilde{w}$ represent the mean velocity motion in the cross-sectional plane (seen for instance in figure 10). The coherence of the large-scale motion is quantified by K_c, which is the volume average of the coherent turbulent kinetic energy of the cross-sectional components $\tilde{k}_c$ obtained by the integration formula of (2.8). While K_c is a good measure of coherence for the majority of cases considered here, it will be shown later that there are two cases for which K_c is not a useful measure. The first case applies when the coherent motion involves a strong temporal dynamics leading to a reduction of the coherent velocities $\tilde{v}$ and $\tilde{w}$ by long time averages.

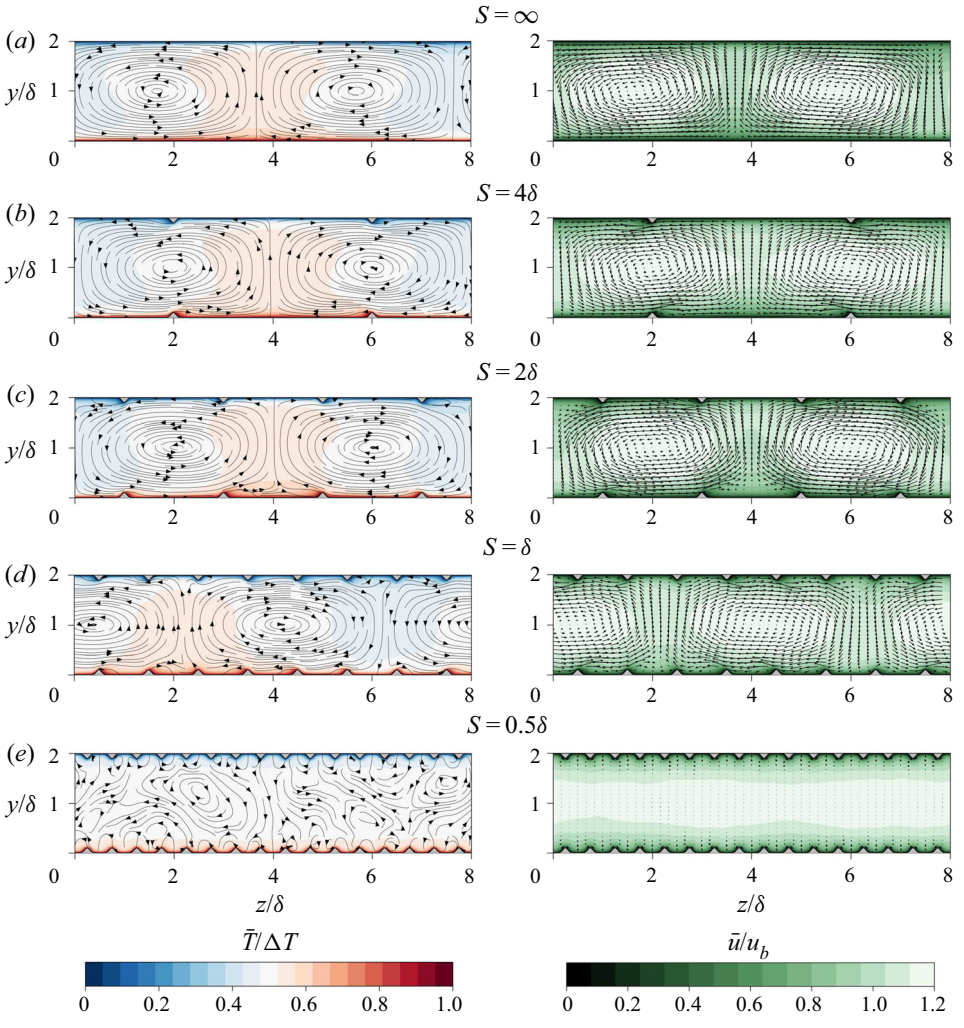

Figure 11. Effect of ridge spacing S on streamwise mean velocity and temperature for constant $Ri_b = 10$.

The second case concerns any coherent motion in the x–y plane, so that this coherence is masked in the random velocity variance contribution.

The influence of the transition between forced convection structures and streamwise rolls on K_c is illustrated in figure 12(a). As can be seen, the forced convection case $Ri_b = 0$ and weakly convective case $Ri_b = 0.003$ for smooth-wall conditions display no coherent energy in the cross-sectional components due to the missing presence of coherent motion. However, the introduction of the Gaussian ridges and the appearance of secondary motions results in a coherent kinetic energy contribution K_c with the highest value for a ridge spacing of $S = \delta$, consistent with recent studies (Medjnoun *et al.* 2020; Wangsawijaya *et al.* 2020). At $Ri_b = 0.016$ the streamwise rolls emerge for the smooth-wall case, which is reflected by an increase of K_c. This increase induced by the streamwise rolls is eventually also present for ridge spacings $S = 4\delta$ and $S = 2\delta$ for case $Ri_b = 0.024$. As shown in the previous sections, the two densest ridge spacing cases display secondary motions at higher Ri_b, which leads to an unchanged and constant value of K_c up to $Ri_b = 0.024$ for $S = \delta$

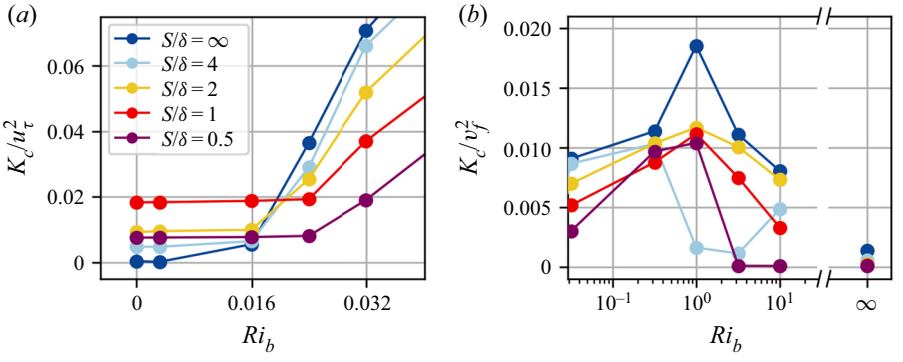

Figure 12. Volume-averaged coherent turbulent kinetic energy of the cross-sectional components for low Ri_b cases scaled in wall units in (a) and for large Ri_b cases scaled in free-fall units in (b).

and $S = 0.5\delta$. This behaviour is consistent with the observation of the delayed increase in Nu with increasing Ra for these two cases in figure 4(a), illustrating the importance of the flow structures in the scaling of global quantities. Due to the presence of streamwise rolls for all cases at $Ri_b = 0.032$, K_c also increases for all S, whose values almost double compared with $Ri_b = 0.024$.

The change of coherence due to the transition between streamwise rolls and convective cells with increasing Ri_b is shown in figure 12(b). For this range of values Ri_b, K_c is scaled in free-fall units, which eases the comparison with the natural convection case $Ri_b = \infty$. For the smooth-wall condition the coherence increases up to $Ri_b = 1$ and subsequently decreases to the natural convection case. This maximum of K_c occurs for a value of $-\delta_{eff}/L = 1.23$, which is consistent with recent findings in ABL, for which the maximum coherence of streamwise rolls is found at $-z_i/L = 1.08$ (Jayaraman & Brasseur 2021). For the rough-wall cases the coherence decreases monotonically with decreasing S only for $Ri_b = 0.032$ and $Ri_b = \infty$, while this behaviour is not found for values in between. Comparing with the smooth-wall cases the introduction of coarsely spaced ridges $S = 4\delta$ yields a large drop of K_c for $Ri_b = 1$ and $Ri_b = 3.2$. The reason for this reduction is the aforementioned temporal variability of the streamwise rolls, which causes the up- and downdrafts to slowly move in the spanwise direction over a long period of time instead of being fixed, thereby reducing averaged values of $\tilde{v}$ and $\tilde{w}$ and thus K_c. This will be discussed in more detail in § 3.5.

For $Ri_b = 10$ the value of K_c for $S = 4\delta$ is below $S = 2\delta$, indicating that the coherence of the streamwise roll is more affected by the coarser ridge spacing. In this case, the reduction of K_c is not related to time variability of the streamwise rolls, but to the relative position of the ridges to the up- and downdrafts. As can be seen in figure 11 the up- and downdrafts for $Ri_b = 10$ occur between the ridges, which for $S = 4\delta$ results in the roll encountering a ridge in the middle of its lateral motion, which causes stronger lateral drag and thereby weakens the roll motion. For $S = 2\delta$, the ridges do not interfere with the roll motions at their strongest lateral velocity. Instead, the adjacent ridges at the up- and downdrafts support the upward motion of the roll by its wall-normal deflection at the ridges. Even though denser ridge spacings contribute to more drag, the support of the deflections compensates in part for the losses in K_c for $S = 2\delta$, while this does not occur for $S = 4\delta$.

For $Ri_b = 3.2$ and $Ri_b = 10$ the value of K_c vanishes for the densest ridge spacing $S = 0.5\delta$, which reflects that streamwise rolls are not present for these cases, as can be seen in the instantaneous temperature fields in figure 6. Also, for the natural convection case,

the value of K_c approaches zero for $S \leq 2\delta$, even though the instantaneous temperature fields in figure 6 suggest an increase of the coherence in the x-direction due to rolls aligned in the z-direction. This reflects the property of K_c that only coherent motion in the z-direction can be detected, while any coherence in the x-direction is masked. Consequently, for the current ridge cases, a reduction of S leads to a weakening of the coherence in the z-direction, which is equivalent to a weakening of rolls with orientation in the x-direction. Note that, for a further reduction of S down to the limit of $S \to 0$, the surface will approach a smooth wall again with a reduced cross-sectional area. Since Re_b and Ra are kept constant while varying S we expect the flow for $S \to 0$ to be similar to the present smooth-wall case $S = \infty$.

The strength of the different large-scale coherent motions is associated with different wall-normal regions, where coherence is dominant. This is shown for the transition between the forced convection structures and streamwise rolls for the horizontally averaged velocity stresses and temperature variance in figure 13 for three different Ri_b cases. The dashed line represents the Reynolds stresses (e.g. $\langle \overline{u'u'} \rangle$), while the solid line indicates the coherent stress (e.g. $\langle \tilde{u}\tilde{u} \rangle$). The difference of both contributions results in the random stress, e.g. $\langle \overline{u''u''} \rangle = \langle \overline{u'u'} \rangle - \langle \tilde{u}\tilde{u} \rangle$. For the forced convection case $Ri_b = 0$ and rough-wall condition the coherent streamwise stress $\langle \tilde{u}\tilde{u} \rangle$ is concentrated close to the wall, with increasing peak values with decreasing S down to $S = \delta$. The densest ridge spacing $S = 0.5\delta$ has a similar peak value as $S = \delta$, however, extending less into the bulk region, consistent with the reduced spatial extent of the mean secondary motions for this ridge spacing seen in figure 9. This is also reflected in the wall-normal location of the peak values of $\langle \tilde{v}\tilde{v} \rangle$ and $\langle \tilde{w}\tilde{w} \rangle$, which are located closer to the wall for $S = 0.5\delta$. The coherent temperature variance displays a similar trend to $\langle \tilde{u}\tilde{u} \rangle$ with respect to S, since temperature is a passive scalar for this case resulting in a strong correlation between the streamwise velocity and temperature.

As discussed before, streamwise rolls are present for case $Ri_b = 0.024$ and $S = \infty, 4\delta, 2\delta$, which can be seen most clearly by increased values of $\langle \tilde{T}\tilde{T} \rangle$ and $\langle \overline{T'T'} \rangle$ within the entire bulk region in figure 13(k). For these cases the coherent temperature variance $\langle \tilde{T}\tilde{T} \rangle$ contributes a large fraction of the temperature variance $\langle \overline{T'T'} \rangle$, which reflects the strong bulging of the mean temperature seen in figure 10(c). The induced coherence by streamwise rolls is also seen in the coherent velocity stresses but is less pronounced. Among them, this is most noticeable for the spanwise coherent velocity stress $\langle \tilde{w}\tilde{w} \rangle$ in figure 13(h), where stronger spanwise coherent stresses are observed with respect to the forced convection cases (figure 13g). A slight increase of $\langle \tilde{u}\tilde{u} \rangle$ and $\langle \tilde{v}\tilde{v} \rangle$ can be also found for these cases in the bulk region, which is illustrated by the insets in figure 13(b,e). Although the coherent velocity stresses of the streamwise rolls are for this case rather weak, this motion is sufficient to cause a strong imprint in the coherent temperature variance. For the two densest ridge spacings $S = \delta$ and $S = 0.5\delta$ where secondary motions occur, the velocity stresses and temperature variances remain similar to the forced convection cases at $Ri_b = 0$. This further supports the fact that the increased drag and vertical mixing due to the ridges for these two cases are strong enough to inhibit the formation of streamwise rolls.

For case $Ri_b = 0.032$, when all ridge configurations exhibit streamwise rolls, the two densest ridge spacings S now also show a significant increase in the coherent temperature variance $\langle \tilde{T}\tilde{T} \rangle$, although their values are lower than for the streamwise roll cases of $Ri_b = 0.024$. Likewise, the increase of coherent velocity stresses, which was initiated at $Ri_b = 0.024$, continues, which is clearly seen by $\langle \tilde{w}\tilde{w} \rangle$ in figure 13(i). As can be seen, the

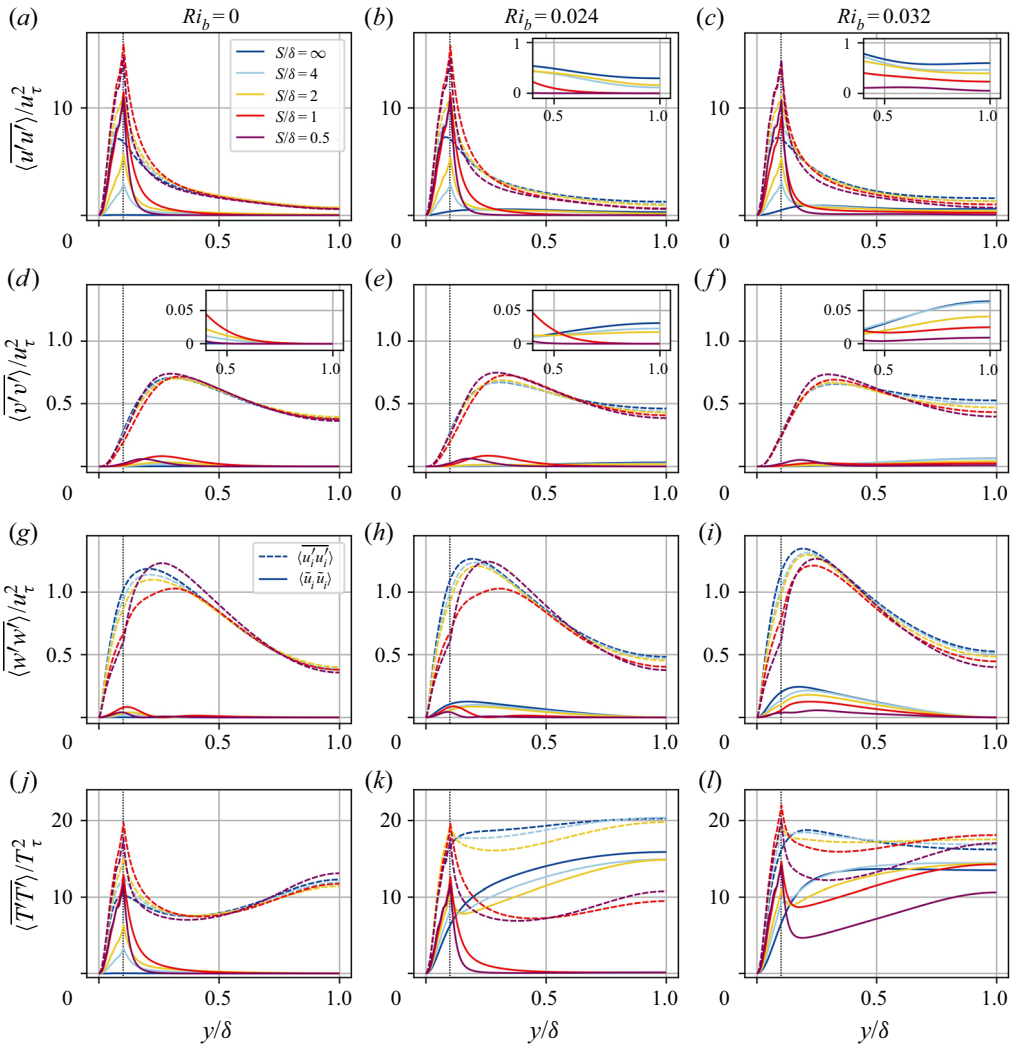

Figure 13. Velocity and temperature variances scaled in inner units for low bulk Richardson number Ri_b cases at transition from forced convection structures to streamwise rolls. Black vertical dotted line indicates the height of the Gaussian ridges.

successive reduction of the ridge spacing S results in a decrease of the coherent velocity stresses, indicating that the streamwise rolls are damped by the presence of the ridges. For $S = 0.5\delta$ only a mild increase of $\langle \tilde{u}\tilde{u} \rangle$ and $\langle \tilde{v}\tilde{v} \rangle$ is found in the bulk region (figure 13*c*,*f*), and the near-wall peak of $\langle \tilde{v}\tilde{v} \rangle$, introduced by the secondary motions, is still visible. The persistence of stronger wall-normal coherent motions near the wall for $S = 0.5\delta$, similar to the forced convection cases, is consistent with the streamwise rolls to appear more spot like, as seen in figure 6.

Figure 14 shows the velocity stresses and temperature variance for the transition from streamwise rolls to natural convection. For case $Ri_b = 1$ the streamwise roll displays the strongest coherent cross-sectional motion, which is illustrated by larger values of $\langle \tilde{w}\tilde{w} \rangle$ compared with the $\langle \tilde{u}\tilde{u} \rangle$. At the same time the wall-normal Reynolds stresses have comparable magnitude to the streamwise Reynolds stress in the channel centre region.

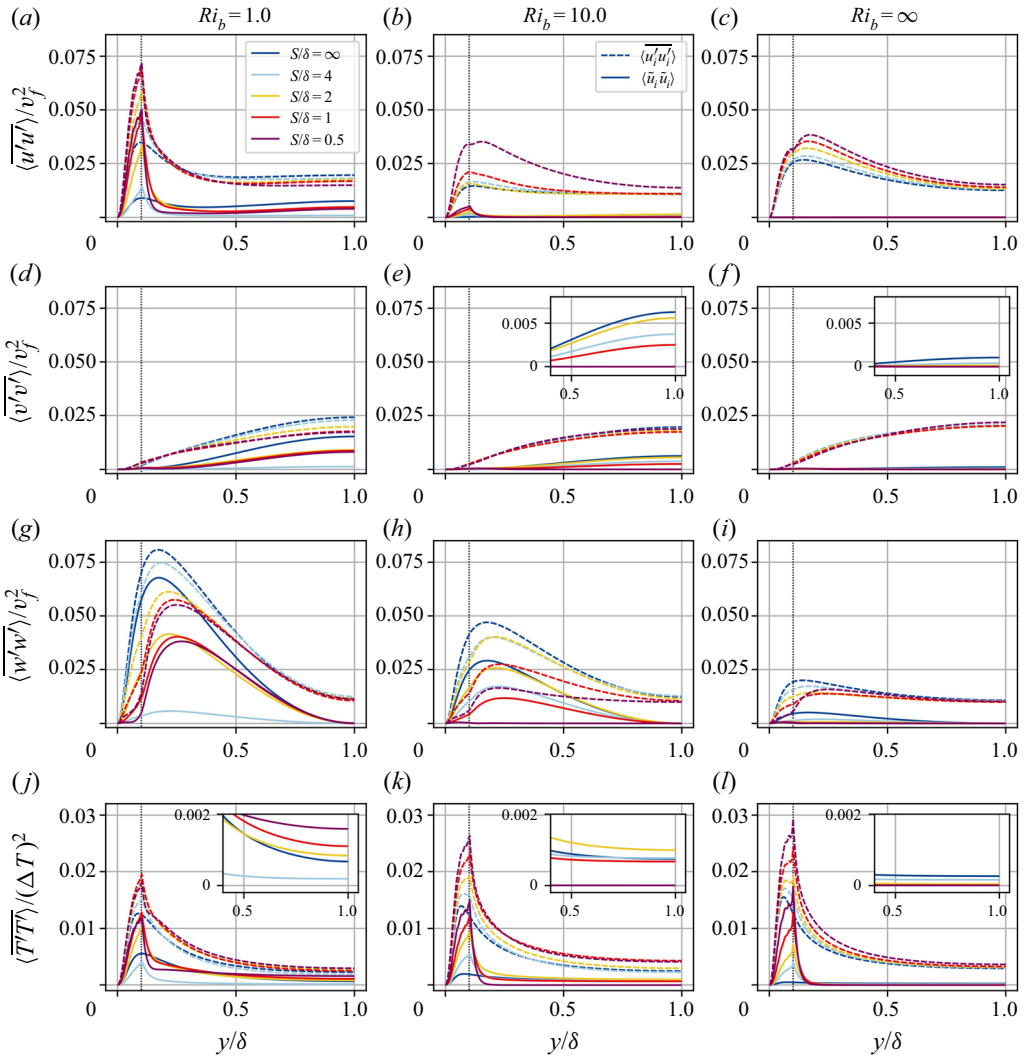

Figure 14. Velocity and temperature variances scaled in free-fall units for high bulk Richardson number Ri_b cases at transition from streamwise rolls to natural convection.

The decrease of coherent velocity stresses with decreasing S is found for the three densest ridge spacings, while case $S = 4\delta$ displays significantly lower values due to the time variability of the streamwise rolls. At the same time, the coherent temperature variance in the bulk region increases with decreasing S (inset figure 14*j*) and $\langle \overline{T'T'} \rangle$ exhibits larger values in the near-wall region compared with the smooth-wall case.

As discussed in relation to figure 12, the coherence of streamwise rolls is reduced when increasing Ri_b beyond values of $Ri_b \approx 1$, which is reflected in a reduction of the coherent velocity stresses for $Ri_b = 10$. For $Ri_b = 10$ and dense ridge spacings $S = \delta$ and $S = 0.5\delta$ the instantaneous temperature fields in figure 6 show a transition from the streamwise rolls to convection cells, which is reflected here in significant lower coherent stresses $\langle \tilde{v}\tilde{v} \rangle$ and $\langle \tilde{w}\tilde{w} \rangle$ compared with the smooth-wall case. The increased peak value of $\langle \overline{T'T'} \rangle$ with decreasing S indicates that ridges are more efficient in mixing temperature close to the

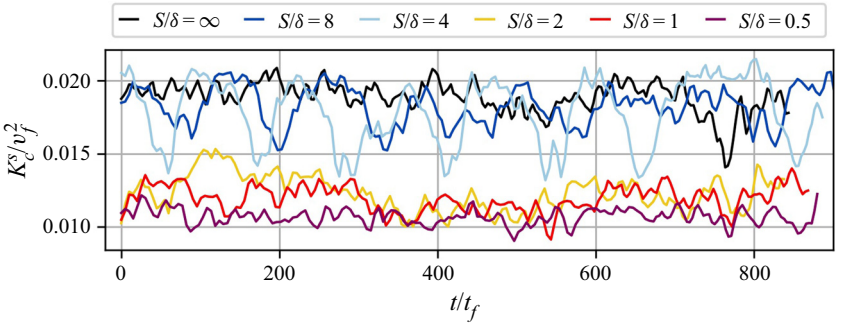

Figure 15. Short-time-averaged coherent kinetic energy K_c^s of case $Ri_b = 1$ and different ridge spacings over time. The values of K_c^s are averaged for time intervals $\Delta t_s \approx 3.4t_f$.

wall. For the densest ridge spacing $S = 0.5\delta$ the convection cells are oriented along the spanwise direction, which is in agreement with the observation of zero coherent spanwise stresses $\langle\tilde{w}\tilde{w}\rangle$ in figure 14(*h*).

The observation that the coherence of convective cells oriented along the x-direction is significantly reduced for $S \leq 2\delta$ is also reflected in the coherent velocity stresses and coherent temperature variance. The coherent contribution of $\langle\tilde{w}\tilde{w}\rangle$ for $S = 4\delta$ is significantly reduced compared with smooth-wall conditions, as can be seen in figure 14(*i*). The only increase of coherence can be found for $\langle\tilde{T}\tilde{T}\rangle$ in the near-wall region with decreasing S in figure 14(*l*), while it vanishes in the bulk region for dense spacings. The preferred orientation of the convective cells in the spanwise direction, as seen in figure 6, needs to result in larger streamwise motion, which is reflected in the steady increase of $\langle\overline{u'u'}\rangle$ with S (figure 14*c*). This is also accompanied by a steady increase of $\langle\overline{T'T'}\rangle$ with decreasing S, which suggests that the aligned ridges induce stronger thermal plumes. Note that, in a square domain with smooth-wall conditions, the streamwise and spanwise stresses have the same distributions due to the directional invariance of the cells (Pandey, Scheel & Schumacher 2018). However, the smooth-wall case already displays slightly larger values for $\langle\overline{u'u'}\rangle$ than $\langle\overline{w'w'}\rangle$ and this indicates that the convection cells are slightly more oriented in the spanwise direction before introducing the aligned ridges.

3.5. *Variability of streamwise rolls*

In the previous section it was found that the coherence of the streamwise rolls for coarse ridge spacings $S = 4\delta$ drops significantly for case $Ri_b = 1$ and $Ri_b = 3.2$ compared with the denser values of S, indicating weaker cross-sectional motion of the roll. However, the instantaneous temperature visualisations in figures 6 and 7 for this specific case do not indicate weaker streamwise rolls, suggesting that a time-varying behaviour of the streamwise rolls might be present. For this purpose, the volume-averaged coherent turbulent kinetic energy of the cross-sectional components K_c, which is based on the average of the entire time series, is now averaged for shorter time windows. The short-time-averaged coherent turbulent kinetic energy K_c^s (superscript s indicates the short-time average) is computed over a time range of $\Delta t_s \approx 3.4t_f$. Note that the value of the short-time average is the shortest available data for the present simulations. The time evolution of K_c^s for consecutive short-time intervals is shown for case $Ri_b = 1$ in figure 15. As can be seen, all cases feature a relatively slow dynamics and for $S = \infty$ and $S \leq 2\delta$ the time variations vary mildly around their full time-averaged values K_c in

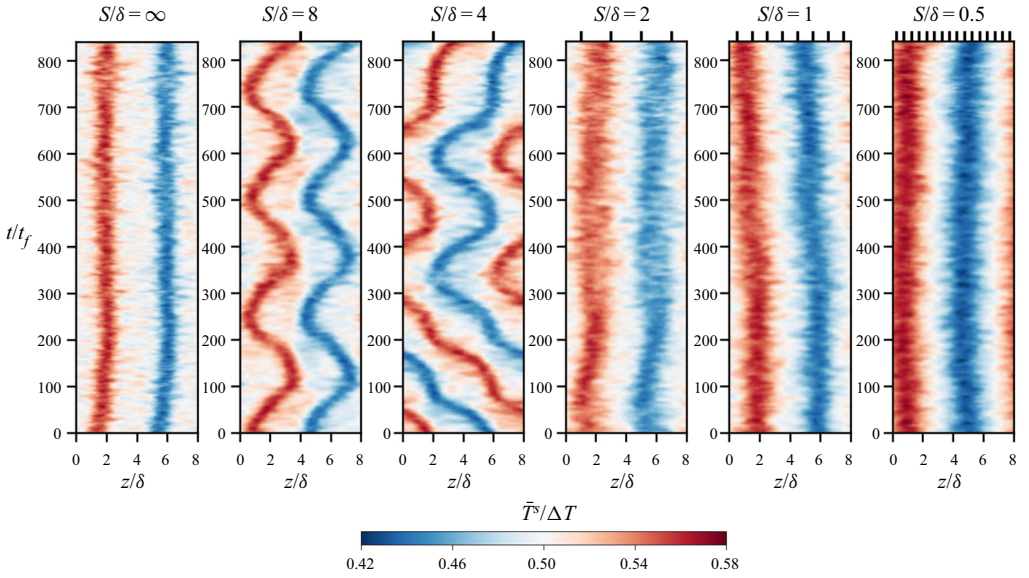

Figure 16. Streamwise- and short-time-averaged temperature $\overline{T}^s$ over time and spanwise position at the wall-normal channel centre location $y = \delta$ for cases $Ri_b = 1$. The spanwise position of the ridges is indicated by the black lines on the top panels.

figure 12(*b*). For $S = 4\delta$ the time variation is more pronounced and the dynamics shows a clearly visible periodic reduction of K_c^s with a period of $O(t) \approx 100t_f$, which corresponds to $O(t) \approx 200t_b$. For this analysis an additional simulation with $S = 8\delta$ is performed and it shows similar time variation compared with $S = 4\delta$, however, with smaller amplitude. This observed dynamics is significantly slower than observations in ABL where the dynamics of the flow reaches a statistically quasi-steady state in roughly $6t_f$ (Moeng & Sullivan 1994). The time mean value of K_c^s is significantly larger than the value K_c, which suggests that the streamwise rolls of $S = 4\delta$ and $S = 8\delta$ feature some time variability, which is masked by considering quantities based on the average of the entire time series. This time-varying behaviour is also found for $Ri_b = 3.2$ and $S = 4\delta$, which also displayed a significant reduction of K_c in figure 12.

The variability of the streamwise rolls is illustrated by the time evolution of the short-time- and streamwise-averaged temperature $\overline{T}^s$ at the wall-normal channel centre $y = \delta$ along the spanwise direction z in figure 16. The spanwise position of the thermal up- and downdrafts of the streamwise roll is represented by the higher and lower temperature values, respectively. While the spanwise location of the up- and downdrafts remain at the same position for $S = \infty$ and $S \leq 2\delta$, the spanwise location of the up- and downdrafts of case $S = 4\delta$ and $S = 8\delta$ is strongly varying in time. The up- and downdrafts for these two cases exhibit strong lateral movement. While this movement is almost periodic for $S = 8\delta$ and remains between the ridges, the up- and downdrafts of $S = 4\delta$ are able to cross the ridges at some time instances, e.g. $t/t_f \approx 100$, while they are not able to cross them at other time instances, e.g. $t/t_f \approx 350$. The large values of K_c^s of $S = 4\delta$ and $S = 8\delta$ in figure 15 correspond to occasions when the up- and downdrafts are located close to or directly at the ridges, e.g. $t = 700$–$800t_f$, while small values of K_c^s correspond to locations of the up- and downdrafts in between the ridges. This increase of K_c^s can be interpreted by the formation mechanism of streamwise rolls proposed by Khanna & Brasseur (1998), which relates them to the organisation of localised buoyancy forces

within near-wall streaks. When the up- and downdrafts are located at ridges, the ridges support the formation of strong localised buoyancy forces, leading to strong local up- and downdrafts. Due to the symmetric arrangement of the ridges at both walls, the up- and downdrafts impinge at another ridge on the opposite wall, which is supposed to counteract the impinging roll by the formation of localised buoyancy forces with opposing direction. Thus, for $S = 4\delta$ the ridges support the formation of strong up- and downdrafts, however, they cannot remain at the spanwise location due to the counteraction of the opposing ridge, leading to the lateral evasion. For case $S = 8\delta$ this enhancement at the ridges occurs only for the up- or the downdraft and not simultaneously as for $S = 4\delta$, which might be an explanation for the observation that up- and downdrafts are not able to cross the ridges.

For case $S = 2\delta$ a short-time interval $t \approx 120t_f$ with large values of K_c^s is present, which corresponds to a time interval in which the up- and downdrafts are located above ridges. However, most of the time the up- and downdrafts remain in between adjacent ridges, as has been shown in figure 11, and only a slight meandering within this range is observed. The examination of time series of cases $Ri_b = 0.32$ and $Ri_b = 10$ does not reveal this strong lateral movement of the up- and downdraft locations, while for $Ri_b = 3.2$ and $S = 4\delta$ a similar lateral movement is found. The results suggest that the dynamics of the streamwise rolls is very sensitive to ridge spacings of the order of the spanwise rolls' width, as seen for $S = 4\delta$ and $S = 8\delta$. For denser ridge spacings $S \leq 2\delta$ several adjacent ridges contribute by localised buoyancy forces to the formation of the up- and downdrafts which might be strong enough to inhibit disturbances by the opposing ridges and thereby prevent lateral movement of the streamwise rolls. Future investigations with a staggered ridge arrangement or ridges placed only at the bottom or top wall might further shed light on the influence of ridges on the roll formation. For instance, the comparison of a symmetric and staggered arrangement of streamwise-aligned ridges in forced convection flows (Stroh *et al.* 2020*a*) has shown that a staggered arrangement promotes the coherence of the large-scale secondary motion, which might also be valid for rolls and may lead to a fixation of the rolls for $S = 4\delta$.

3.6. *Reynolds number effects*

In the previous section the flow organisation of mixed convection flows was considered in terms of varying bulk Richardson number Ri_b and ridge spacing S, while the Reynolds number Re_k was approximately constant. The effect of Re_k on the transition between forced convection structures and streamwise rolls is shown in figure 17, which presents the cross-sectional mean temperature and flow topology for case $Ri_b = 0.024$ with values of $Re_k = 252$–263 and case $Ri_b = 0.025$ with threefold larger values of $Re_k = 826$–841. As can be seen figure 17(*a*) both cases feature a streamwise roll down to a ridge spacing of $S = 2\delta$ (not shown for $S = \infty$ and $S = 4\delta$). The comparison of the temperature fields between the low and high Re_k cases depicts that the thermal boundary layer is reduced for higher Re_k due to the more efficient mixing of the flow in the near-wall region. As shown in the previous sections, the streamwise rolls are replaced by secondary motions for the lower Re_k cases with $Ri_b = 0.024$ and $S \leq \delta$, while for the larger Re_k cases the streamwise roll remains for these ridge spacings. However, the streamwise roll appears more distorted and affected by the ridges, as can be seen for $S = \delta$ and $S = 0.5\delta$. In addition, secondary motion in the form of one pair of counter-rotating vortices emerges at one ridge at the bottom wall lying in the downdraft region of the roll. This illustrates that the ridges on the opposing wall of the up- and downdraft regions are able to form coherent structures that counteract the large-scale roll formation. For the densest ridge

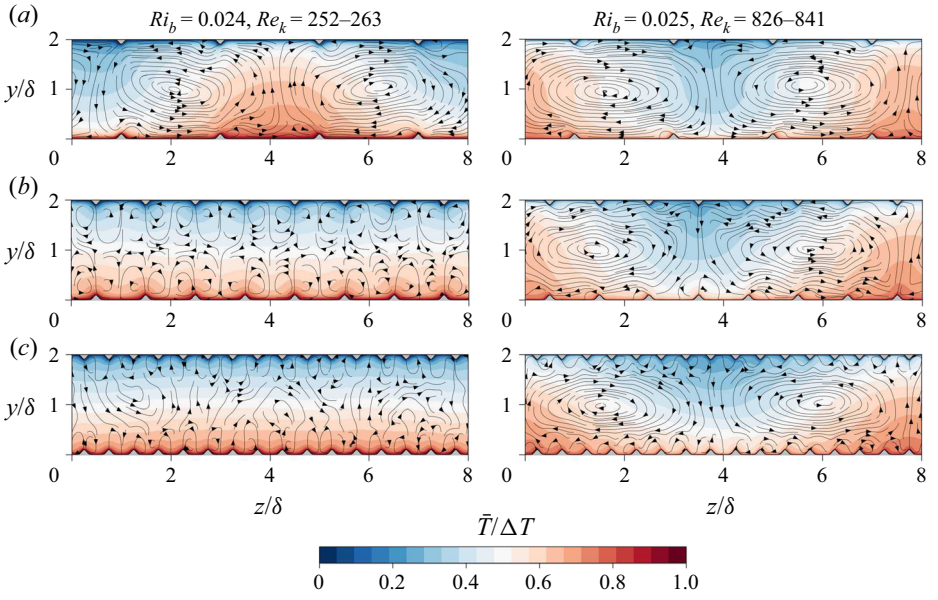

Figure 17. Effect of turbulent Reynolds number Re_k and spanwise ridge spacing S on mean temperature for case $Ri_b = 0.024$, $Re_k = 252$–263 ($Ra = 7.5 \times 10^5$, $Re_b = 2800$) on the left side and case $Ri_b = 0.025$, $Re_k = 826$–841 ($Ra = 10^7$, $Re_b = 10\,000$) on the right side. The spanwise spacing of the Gaussian ridges is $S = 2\delta$ (a), $S = \delta$ (b) and $S = 0.5\delta$ (c).

spacing $S = 0.5\delta$ in figure 17(c) the streamwise roll for the large Re_k case is now confined to a smaller wall-normal region in the bulk flow. This is associated with the recirculation zones at the leeward side of the ridges, which are connected between the up- and downdraft regions, thereby forming a roughness sublayer which inhibits the attachment of the lateral movement of the streamwise roll at the wall. These results suggest that the transition range between forced convection structures and streamwise rolls with heterogeneous rough surfaces is not solely determined by the pair of Ri_b and S, but also by the value of the Reynolds number Re_k. Due to the increased turbulent mixing for larger values of Re_k the streamwise rolls can counteract the additional shear by the ridges, such that the transition between forced convection structures and streamwise rolls is shifted towards smaller values of Ri_b.

The influence of Re_k on the roll-to-cell transition is illustrated for two cases with $Ri_b = 3.2$ and different Re_k by the temperature fluctuation in the horizontal mid-plane in figure 18. As can be seen, both cases exhibit streamwise rolls for smooth-wall conditions and $S \geq 2\delta$, while differences in the flow structures start to appear at $S = \delta$. At this ridge spacing the lower Re_k case still shows streamwise rolls (figure 18a), while for the larger Re_k case the streamwise rolls are disturbed by strong thermal plumes spanning almost the entire spanwise domain. For the lower Re_k case with $S = 0.5\delta$ no coherent streamwise rolls can be observed and, similar to $S = \delta$, for the larger Re_k case thermal plumes emerge, which indicates the beginning of the transition to convective cells. This shows that increasing Re_k has a comparable effect on the flow organisation to the reduction of the ridge spacing S. While smaller values of S increase the friction of the flow and weaken the lateral motion of the streamwise rolls, the higher Re_k increases the thermal mixing near the wall, and both effects promote the formation of thermal plumes. The loss of coherence of the streamwise rolls for case $S = 0.5\delta$ in figure 18(a) is also supported by a vanishing value of K_c in figure 12(b). Also the inspection of the time series of K_c^s reveals only a very weak

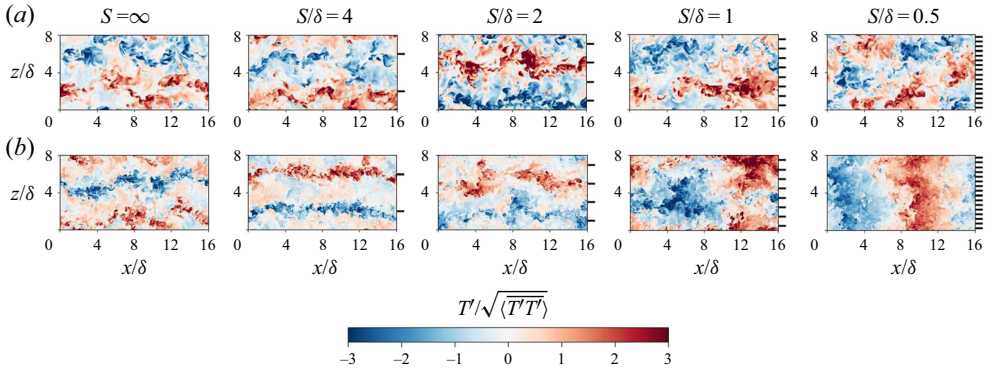

Figure 18. Instantaneous temperature fluctuation fields at the half-channel height position $y = \delta$ for cases $Ri_b = 3.2$ with $Re_k = 236$–263 ($Ra = 10^7$, $Re_b = 885$) in (a) and $Re_k = 695$–792 ($Ra = 10^8$, $Re_b = 2800$) in (b) for different spanwise ridge spacings S.

contribution, which is an order magnitude lower than for case $S = \delta$. The observation that only convective cells with preferential orientation in the z-direction occur for the natural convection cases $S \leq 2\delta$ and for $Ri_b = 10$ with $S = 0.5\delta$ is also seen for the large Re_k case with $S = 0.5\delta$. The influence of Re_k on the transition between streamwise rolls and convective cells is such that higher values of Re_k initiate this transition to convective cells at smaller Ri_b, thus reducing the range of streamwise rolls.

4. Discussion and conclusion

The present study shows that heterogeneous surfaces in form of streamwise-aligned Gaussian ridges have a significant influence on the flow organisation of mixed convection flows. The appearance of streamwise rolls is considerably reduced for dense ridge spacings S, which is related to the increased drag introduced by the ridges. Therefore, the formation of the rolls requires larger buoyancy forces, such that the transition from forced convection structures to streamwise rolls is delayed by the ridges towards higher Ri_b values than expected for smooth-wall conditions. Specifically, this transition occurs for the smooth channel at $Ri_b = 0.016$, while for large ridge spacings of $S \geq 2\delta$ this transition occurs first at $Ri_b = 0.024$ and for denser ridge spacings $S \leq \delta$ at $Ri_b = 0.032$.

The strongest influence of the heterogeneous surface on the flow organisation occurs between the roll-to-cell transition range, where a change of the surface properties has a comparable effect to a change of Ri_b for homogeneous wall conditions. This behaviour is observed by the inspection of the instantaneous and mean cross-sectional velocity and temperature fields. In the range of $Ri_b = 3.2$–10, where streamwise rolls are present for smooth-wall conditions, dense ridge spacings already trigger the transition from roll to cell structures. This is surprising, since this range of bulk Richardson number, which corresponds to a range of stability parameter $-\delta_{eff}/L = 3.4$–9.7, is below the range where commonly cell structures are observed in the ABL (Salesky *et al.* 2017). The results show that the increased lateral drag introduced by the densely spaced ridges diminishes the coherence of the streamwise rolls, and eventually leads to the transition to convective cells at smaller Ri_b. In addition to the earlier roll-to-cell transition the ridges also affect the orientation of the convection cells for denser ridge spacings. While the convective cells have no preferential orientation for the smooth-wall natural convection case, they increasingly prefer to orient perpendicular to the ridges with decreasing S. This is also explained by the additional drag, which is experienced by ridge-aligned convective cells,

such that the lateral near-wall motion of these cells is increasingly disturbed for smaller S. This will eventually lead to their breakdown and the flow prefers to stream only along the ridges, resulting in the occurrence of spanwise coherent convective cells.

For the moderate values of Reynolds numbers that can be afforded for the present simulations, we find that an increase in Re favours the transition from forced convection structures to streamwise rolls at smaller Ri_b, which is associated with the increased thermal vertical mixing at larger Re. At the roll-to-cell transition range, an increase of Re promotes the transition towards convective cells, such that convective cells appear for larger S if Re is increased.

One particular observation is that the dynamics of streamwise rolls is very sensitive to ridge spacings of the order of the rolls' width, which is found for $Ri_b = 1$ and $Ri_b = 3.2$. For the specific ridge spacing $S = 4\delta$ the up- and downdraft regions move over the entire channel slowly in time, with time periods of approximately 100 free-fall time units or 200 time bulk units, which is in contrast to denser ridge spacings and smooth-wall conditions, where the spanwise location of the rolls is fixed. Due to this variation of streamwise rolls in the former case, some statistical features of the rolls are masked by long time integration. This is seen for example for the strength of the roll's coherence, which almost vanishes for long time intervals. Inspection of consecutive short-time averages reveals that the strength of the roll's coherence depends on the spanwise location of the up- and downdraft regions. The coherence is reduced if the up- and downdraft regions occur in the valley of adjacent ridges, and is increased if they occur in the vicinity of the ridges. In the former case the rolls experience stronger lateral drag due to their horizontal movement above the ridges, while in the latter case the ridges support the formation of localised buoyancy forces at the ridges, which in turn strengthens the up- and downdraft regions. Although the ridges reinforce the rolls, they do not reside there permanently. This is likely due to the symmetric arrangement of the ridges at both walls, since the up- and downdrafts impinge on an opposing ridge, which disturbs the roll formation. While the formation mechanism of streamwise rolls is still not clear and under debate (Etling & Brown 1993; Salesky *et al.* 2017), the present observations indicate that the formation and the dynamics of streamwise rolls are very sensitive to heterogeneous surfaces.

Acknowledgements. This work was performed on the computational resources of HOREKA and used the storage facility LSDF funded by the Ministry of Science, Research and the Arts Baden-Württemberg, and Deutsche Forschungsgemeinschaft (DFG) within the framework programme bwHPC.

Funding. K.S. and B.F. acknowledge funding through DFG project number 423710075. J.P.M. acknowledges support through project PID2019-105162RB-I00 funded by MCIN/AEI/10.13039/501100011033.

Declaration of interests. The authors report no conflict of interest.

Data availability statement. Mean statistics of all simulations are published as open-access dataset in the KITopen repository, DOI: https://doi.org/10.5445/IR/1000149685.

Author ORCIDs.
Kay Schäfer https://orcid.org/0000-0002-1704-8233;
Bettina Frohnapfel https://orcid.org/0000-0002-0594-7178;
Juan Pedro Mellado https://orcid.org/0000-0001-7506-6539.

Author contributions. K.S. designed the computational framework, carried out the numerical simulations, performed the data post-processing and statistical analysis with supervision by B.F. and J.P.M. All authors contributed to the conceptualisation of the study as well as to the discussion and interpretation of the data. K.S. wrote the original draft of the paper with review and editing support from B.F. and J.P.M. Funding was acquired by B.F.

Ra	Re_b	Ri_b	S/δ	$N_x \times N_y \times N_z$	C_f	$C_{f,ref}$	ε_{C_f}	Nu	Nu_{ref}	ε_{Nu}
10^6	0	∞	∞	$512 \times 193 \times 256$	—	—	—	8.257	8.288	0.38 %
10^6	158.1	10	∞	$512 \times 193 \times 256$	0.0719	0.0745	3.49 %	7.284	7.318	0.46 %
10^6	500	1	∞	$512 \times 193 \times 256$	0.0267	0.0277	3.69 %	6.312	6.356	0.70 %
10^6	1581	0.1	∞	$512 \times 193 \times 256$	0.0100	0.0102	1.79 %	6.798	6.780	0.26 %
10^6	5000	0.01	∞	$1024 \times 257 \times 512$	0.00712	0.00715	0.39 %	12.360	12.419	0.48 %
10^7	0	∞	∞	$1024 \times 257 \times 512$	—	—	—	15.687	15.799	0.71 %
10^7	500	10	∞	$1024 \times 257 \times 512$	0.0403	0.0403	0.06 %	13.921	14.000	0.56 %
10^7	1581	1	∞	$1024 \times 257 \times 512$	0.0144	0.0146	1.28 %	11.911	11.880	0.26 %
10^7	5000	0.1	∞	$1024 \times 257 \times 512$	0.00742	0.00754	1.63 %	17.112	17.250	0.80 %

Table 2. Simulation parameters and global flow properties of validation study for Rayleigh–Bénard and mixed convection at $Ra = 10^6$ and $Ra = 10^7$. The skin friction coefficient and Nusselt number of Pirozzoli *et al.* (2017) are given by $C_{f,ref}$ and Nu_{ref}.

Appendix A. Validation of code implementation

The implementation of the active scalar in Xcompact3d is validated against the Rayleigh–Bénard and mixed convection cases of Pirozzoli *et al.* (2017) at $Ra = 10^6$ and 10^7. For a direct comparison the same grid resolution is used as in Pirozzoli *et al.* (2017), which is given in table 2. The mean differences in skin friction coefficient and Nusselt number with respect to the reference data are indicated by ε_{C_f} and ε_{Nu}. While for the skin friction coefficient the two low Reynolds number cases at $Re = 10^6$ show deviations of up to 3.7 %, this is reduced to below 1.7 % for the higher Rayleigh number cases. The Nusselt number is in very good agreement for both chosen Rayleigh numbers and stays below 0.8 % for all simulation cases. The mean velocity and mean temperature profiles, as well as the variances $\overline{u'u'}$- and $\overline{T'T'}$-profiles, are shown in figure 19 and the comparison with the reference data shows very good agreement between the considered flow cases.

Appendix B. Grid study with Gaussian ridges

The grid resolution requirements for the simulations with Gaussian ridges are studied for different flow configurations to show that the chosen grid resolution is sufficiently fine to capture the investigated flow physics. The grid refinement study is performed for three different flow configurations, namely pure forced convection, mixed convection and pure Rayleigh–Bénard flow. The domain size for this study was reduced to $L_x \times L_y \times L_z = 8\delta \times 2\delta \times 4\delta$ to keep the grid study computationally affordable. In all cases the spanwise spacing of the Gaussian ridges is $S/\delta = 1$, corresponding to four Gaussian ridges at each sidewall. The different grid resolutions of the simulation cases and the resulting global flow properties are given in table 3.

For the pure forced convection case the mean variations in skin friction coefficient and Nusselt number from the coarsest to the finest grid simulation are within a range of 0.5 % and 0.7 %, respectively. The grid refinement does not reveal any significant changes in the mean velocity, temperature and covariance profiles between all considered cases (not shown here). In order to satisfy the grid requirements proposed by Pirozzoli *et al.* (2017) for pure forced convection flows and being conservative with the spanwise grid resolution for the representation of the Gaussian ridges, the grid $N_x \times N_y \times N_z = 256 \times 193 \times 192$ is chosen to be appropriate. This results for the large domain simulation ($L_x \times L_y \times L_z =$

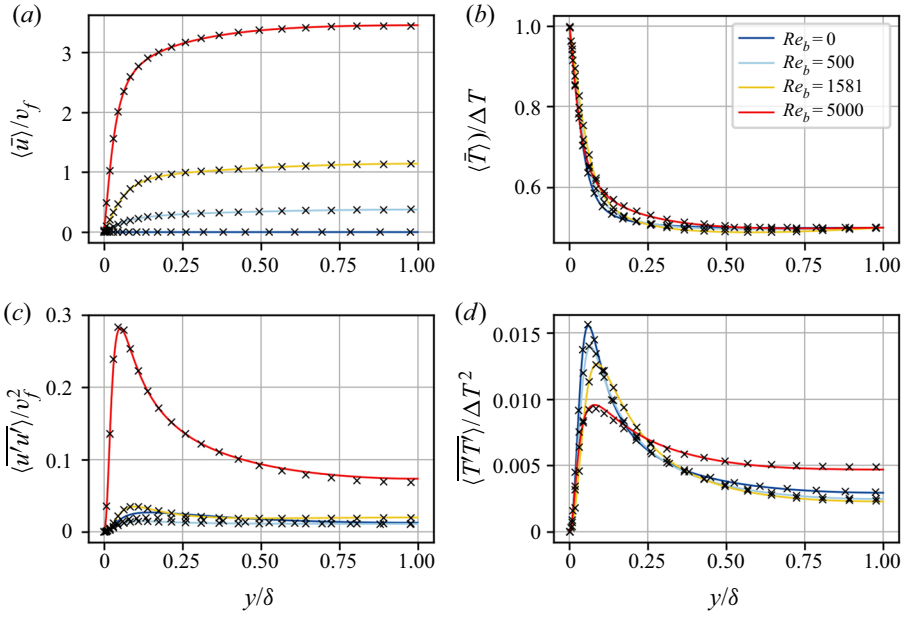

Figure 19. Mean profiles for validation study for $Ra = 10^7$ and different bulk Reynolds numbers. The marks indicate the reference data of Pirozzoli *et al.* (2017), for clarity every fifth data point is shown.

Ra	Re_b	Ri_b	S/δ	$N_x \times N_y \times N_z$	$C_f (\times 10^{-3})$	Nu	$\Delta t_{tot}//t_b$	$\Delta t_{tot}//t_f$
0	2800	0	1	$256 \times 193 \times 128$	8.834	7.991	4719	—
0	2800	0	1	$192 \times 193 \times 192$	8.766	7.957	4719	—
0	2800	0	1	$256 \times 193 \times 192$	8.781	7.958	4719	—
0	2800	0	1	$256 \times 193 \times 256$	8.822	7.997	5271	—
0	2800	0	1	$256 \times 257 \times 192$	8.823	8.014	4719	—
10^7	5000	0.1	1	$512 \times 193 \times 192$	8.265	18.098	5423	864
10^7	5000	0.1	1	$512 \times 193 \times 256$	8.201	18.170	4254	677
10^7	5000	0.1	1	$512 \times 257 \times 192$	8.341	18.216	4301	684
10^7	5000	0.1	1	$512 \times 257 \times 256$	8.194	18.081	4150	660
10^7	5000	0.1	1	$512 \times 257 \times 320$	8.193	18.163	4123	657
10^7	0	∞	1	$512 \times 193 \times 192$	0	16.974	—	1171
10^7	0	∞	1	$512 \times 193 \times 256$	0	16.999	—	1026
10^7	0	∞	1	$512 \times 257 \times 192$	0	16.921	—	1038
10^7	0	∞	1	$512 \times 257 \times 256$	0	17.034	—	1135
10^7	0	∞	1	$512 \times 257 \times 320$	0	16.981	—	1052

Table 3. Grid refinement study for pure forced convection, mixed convection and pure Rayleigh–Bénard flow with Gaussian ridges at each sidewall ($S/\delta = 1$). The domain size for the study is set to $L_x \times L_y \times L_z = 8\delta \times 2\delta \times 4\delta$.

$16\delta \times 2\delta \times 8\delta$) in a grid of $N_x \times N_y \times N_z = 512 \times 193 \times 384$ for pure convection flows with Gaussian ridges.

The grid refinement study for the mixed convection case is performed at $Ra = 10^7$, which requires a finer grid compared with the grid study of the pure forced convection case at $Re_b = 2800$ according to smooth-wall cases (see table 3). Furthermore, we increase the

bulk Reynolds number to $Re_b = 5000$ in order to make this grid study more demanding in terms of the requirements of the shear induced turbulence. The mean difference of all cases in C_f and Nu with respect to the finest grid case lies below 1.81 % for the skin friction coefficient and 0.45 % for Nusselt number. This demonstrates, that the grid resolution for the plane wall mixed convection cases is already sufficient for the additional numerical representation of Gaussian ridges by the IBM based on polynomial reconstruction. Similar results are obtained for the pure Rayleigh–Bénard case at $Ra = 10^7$, where the mean difference in Nu with respect to the finest grid case is below 0.35 % for all simulation cases. Consequently, for the investigation of mixed and natural convection at $Ra = 10^7$ a grid of $N_x \times N_y \times N_z = 1024 \times 257 \times 512$ for the large domain cases is chosen. For lower Ra cases, the chosen grid resolution of the pure forced convection study marks the lower bound to sufficiently represent the Gaussian ridges in these cases.

References

Anderson, W., Barros, J.M., Christensen, K.T. & Awasthi, A. 2015 Numerical and experimental study of mechanisms responsible for turbulent secondary flows in boundary layer flows over spanwise heterogeneous roughness. *J. Fluid Mech.* **768**, 316–347.

Awasthi, A. & Anderson, W. 2018 Numerical study of turbulent channel flow perturbed by spanwise topographic heterogeneity: amplitude and frequency modulation within low- and high-momentum pathways. *Phys. Rev. Fluids* **3** (4), 044602.

Barros, J.M. & Christensen, K.T. 2014 Observations of turbulent secondary flows in a rough-wall boundary layer. *J. Fluid Mech.* **748**, R1.

Bartholomew, P., Deskos, G., Frantz, R.A.S., Schuch, F.N., Lamballais, E. & Laizet, S. 2020 Xcompact3D: an open-source framework for solving turbulence problems on a Cartesian mesh. *SoftwareX* **12**, 100550.

Blass, A., Zhu, X., Verzicco, R., Lohse, D. & Stevens, R.J.A.M. 2020 Flow organization and heat transfer in turbulent wall sheared thermal convection. *J. Fluid Mech.* **897**, A22.

Bou-Zeid, E., Anderson, W., Katul, G.G. & Mahrt, L. 2020 The persistent challenge of surface heterogeneity in boundary-layer meteorology: a review. *Boundary-Layer Meteorol.* **177** (2), 227–245.

Chan-Braun, C., García-Villalba, M. & Uhlmann, M. 2011 Force and torque acting on particles in a transitionally rough open-channel flow. *J. Fluid Mech.* **684**, 441–474.

Chung, D., Monty, J.P. & Hutchins, N. 2018 Similarity and structure of wall turbulence with lateral wall shear stress variations. *J. Fluid Mech.* **847**, 591–613.

Colombini, M. 1993 Turbulence-driven secondary flows and formation of sand ridges. *J. Fluid Mech.* **254**, 701–719.

Deardorff, J.W. 1972 Numerical investigation of neutral and unstable planetary boundary layers. *J. Atmos. Sci.* **29** (1), 91–115.

Etling, D. & Brown, R.A. 1993 Roll vortices in the planetary boundary layer: a review. *Boundary-Layer Meteorol.* **65** (3), 215–248.

Gautier, R., Laizet, S. & Lamballais, E. 2014 A DNS study of jet control with microjets using an immersed boundary method. *Intl J. Comput. Fluid Dyn.* **28** (6–10), 393–410.

Hanna, S.R. 1969 The formation of longitudinal sand dunes by large helical eddies in the atmosphere. *J. Appl. Meteorol. Climatol.* **8** (6), 874–883.

Hinze, J.O. 1973 Experimental investigation on secondary currents in the turbulent flow through a straight conduit. *Appl. Sci. Res.* **28** (1), 453–465.

Hwang, H.G. & Lee, J.H. 2018 Secondary flows in turbulent boundary layers over longitudinal surface roughness. *Phys. Rev. Fluids* **3** (1), 014608.

Jayaraman, B. & Brasseur, J.G. 2021 Transition in atmospheric boundary layer turbulence structure from neutral to convective, and large-scale rolls. *J. Fluid Mech.* **913**, A42.

Khanna, S. & Brasseur, J.G. 1998 Three-dimensional buoyancy- and shear-induced local structure of the atmospheric boundary layer. *J. Atmos. Sci.* **55** (5), 710–743.

Laizet, S. & Lamballais, E. 2009 High-order compact schemes for incompressible flows: a simple and efficient method with quasi-spectral accuracy. *J. Comput. Phys.* **228** (16), 5989–6015.

LeMone, M.A. 1973 The structure and dynamics of horizontal roll vortices in the planetary boundary layer. *J. Atmos. Sci.* **30** (6), 1077–1091.

MEDJNOUN, T., VANDERWEL, C. & GANAPATHISUBRAMANI, B. 2018 Characteristics of turbulent boundary layers over smooth surfaces with spanwise heterogeneities. *J. Fluid Mech.* **838**, 516–543.

MEDJNOUN, T., VANDERWEL, C. & GANAPATHISUBRAMANI, B. 2020 Effects of heterogeneous surface geometry on secondary flows in turbulent boundary layers. *J. Fluid Mech.* **886**, A31.

MOENG, C. & SULLIVAN, P.P. 1994 A comparison of shear- and buoyancy-driven planetary boundary layer flows. *J. Atmos. Sci.* **51** (7), 999–1022.

MONIN, A.S. & OBUKHOV, A.M. 1954 Basic laws of turbulent mixing in the surface layer of the atmosphere. *Contrib. Geophys. Inst. Acad. Sci. USSR* **151** (163), e187.

OBUKHOV, A.M. 1946 Turbułence in an atmosphere with inhomogeneous temperaturc. *Tr. Inst. Teor. Geofiz. Akad. Nauk SSSR* **1**, 95–115.

PANDEY, A., SCHEEL, J.D. & SCHUMACHER, J. 2018 Turbulent superstructures in Rayleigh–Bénard convection. *Nat. Commun.* **9** (1), 2118.

PIROZZOLI, S., BERNARDINI, M., VERZICCO, R. & ORLANDI, P. 2017 Mixed convection in turbulent channels with unstable stratification. *J. Fluid Mech.* **821**, 482–516.

SALESKY, S.T., CHAMECKI, M. & BOU-ZEID, E. 2017 On the nature of the transition between roll and cellular organization in the convective boundary layer. *Boundary-Layer Meteorol.* **163** (1), 41–68.

SCAGLIARINI, A., GYLFASON, Á. & TOSCHI, F. 2014 Heat-flux scaling in turbulent Rayleigh–Bénard convection with an imposed longitudinal wind. *Phys. Rev.* E **89** (4), 043012.

SCHERER, M., UHLMANN, M., KIDANEMARIAM, A.G. & KRAYER, M. 2022 On the role of turbulent large-scale streaks in generating sediment ridges. *J. Fluid Mech.* **930**, A11.

SCHÄFER, K., STROH, A., FOROOGHI, P. & FROHNAPFEL, B. 2022 Modelling spanwise heterogeneous roughness through a parametric forcing approach. *J. Fluid Mech.* **930**, A7.

SHAO, Y. 2008 *Physics and Modelling of Wind Erosion*. Atmospheric and Oceanographic Sciences Library, vol. 37. Springer.

STROH, A., SCHÄFER, K., FOROOGHI, P. & FROHNAPFEL, B. 2020*a* Secondary flow and heat transfer in turbulent flow over streamwise ridges. *Intl J. Heat Fluid Flow* **81**, 108518.

STROH, A., SCHÄFER, K., FROHNAPFEL, B. & FOROOGHI, P. 2020*b* Rearrangement of secondary flow over spanwise heterogeneous roughness. *J. Fluid Mech.* **885**, R5.

VANDERWEL, C. & GANAPATHISUBRAMANI, B. 2015 Effects of spanwise spacing on large-scale secondary flows in rough-wall turbulent boundary layers. *J. Fluid Mech.* **774**, R4.

VANDERWEL, C., STROH, A., KRIEGSEIS, J., FROHNAPFEL, B. & GANAPATHISUBRAMANI, B. 2019 The instantaneous structure of secondary flows in turbulent boundary layers. *J. Fluid Mech.* **862**, 845–870.

WANG, Z.-Q. & CHENG, N.-S. 2006 Time-mean structure of secondary flows in open channel with longitudinal bedforms. *Adv. Water Resour.* **29** (11), 1634–1649.

WANGSAWIJAYA, D.D., BAIDYA, R., CHUNG, D., MARUSIC, I. & HUTCHINS, N. 2020 The effect of spanwise wavelength of surface heterogeneity on turbulent secondary flows. *J. Fluid. Mech.* **894**, A7.

WILLINGHAM, D., ANDERSON, W., CHRISTENSEN, K.T. & BARROS, J.M. 2014 Turbulent boundary layer flow over transverse aerodynamic roughness transitions: induced mixing and flow characterization. *Phys. Fluids* **26** (2), 025111.

WYNGAARD, J.C. 2010 *Turbulence in the Atmosphere*. Cambridge Core.

ZAMPIRON, A., CAMERON, S. & NIKORA, V. 2020 Secondary currents and very-large-scale motions in open-channel flow over streamwise ridges. *J. Fluid Mech.* **887**, A17.